

Physical characteristics of glasma from the earliest stage of relativistic heavy ion collisions

Margaret E. Carrington ^{1,2}, Alina Czajka ³, and Stanisław Mrówczyński ^{4,3}

¹*Department of Physics, Brandon University, Brandon, Manitoba R7A 6A9, Canada*

²*Winnipeg Institute for Theoretical Physics, Winnipeg, Manitoba, Canada*

³*National Centre for Nuclear Research, ul. Pasteura 7, PL-02-093 Warsaw, Poland*

⁴*Institute of Physics, Jan Kochanowski University, ul. Uniwersytecka 7, PL-25-406 Kielce, Poland*



(Received 3 June 2021; revised 6 March 2022; accepted 26 July 2022; published 12 September 2022)

We present some analytic results that describe the gluon field, or glasma, that exists at very early times after a collision of relativistic heavy ions at proper time $\tau = 0$. We use a color glass condensate approach, and perform an expansion in τ . The full details of our calculational method are described in our previous paper [Carrington, Czajka, and Mrówczyński, *Eur. Phys. J. A* **58**, 5 (2022)], where we have explained all of the steps that are necessary to obtain the energy-momentum tensor up to sixth order in τ . In this paper we present an analysis of various physical quantities that can be obtained from this energy-momentum tensor. We show that the expansion to order τ^6 can be trusted to about $\tau = 0.05$ fm. We calculate the transverse and longitudinal pressures and show that, for times small enough that the expansion converges, they move towards their equilibrium values of one third of the energy density. We also study the spatial eccentricity of the glasma and the Fourier coefficients of the azimuthal flow. Our results for the Fourier coefficients are larger than expected, which contradicts the usual assumption that anisotropy is mostly generated during the hydrodynamic evolution of the plasma. We find a significant correlation between the elliptic flow coefficient and the eccentricity, which indicates that the spatial asymmetry introduced by the initial geometry is effectively transmitted to the azimuthal distribution of the gluon momentum field, even at very early times. This result is interesting because correlations of this kind are characteristic of the onset of hydrodynamic behavior. Finally, we have calculated the angular momentum of the glasma and obtained results that are many orders of magnitude smaller than the angular momentum of the initial system of colliding ions in a configuration with nonzero impact parameter. This indicates that most of the angular momentum carried by the valence quarks is not transmitted to the glasma. The result is significant because it contradicts the picture of a rapidly rotating initial glasma state that has been proposed by several authors, but agrees with the current lack of experimental evidence for a significant polarization effect of the hyperons and vector mesons produced in heavy ion collisions at the highest accessible energies.

DOI: [10.1103/PhysRevC.106.034904](https://doi.org/10.1103/PhysRevC.106.034904)

I. INTRODUCTION

We use a formulation of the color glass condensate (CGC) effective theory to describe the dynamics of a heavy-ion collision in the early stages after the collision ($\tau \lesssim 1$ fm). Many reviews of the CGC effective theory have been published; see for example [1,2]. The details of the evolution of a quark-gluon plasma (QGP) during this early stage are not well understood, but they are important because they provide the initial conditions for subsequent hydrodynamic evolution. The CGC approach is based on a separation of scales between valence partons with large nucleon momentum fraction and gluon fields with small nucleon momentum fraction. When the separation scale is fixed, the dynamics of the gluon fields can be determined from the classical Yang-Mills (YM)

equation with the source provided by the valence partons, by averaging over an ensemble of valence parton color charge distributions.

This paper is a companion paper to a previous work [3] in which we have explained the strategy of our approach and some details of the calculational method. We use an expansion in the proper time, also called a “near field” expansion [4–8]. We work with infinitely Lorentz contracted sources, and the description of the system is classical. An advantage of the method, however, is that our results are analytic, and thus provide a potentially valuable alternative approach to the various numerical methods that are in use. In Ref. [3] we focused on the technical details of the calculation and showed only a few results, which were obtained for the simple case of nuclei that are infinite in the transverse plane and uniform. In this paper we consider more physically realistic collisions where the nuclear area density function is not assumed constant. We present results from several different calculations and discuss their connection to experimental observables.

In Sec. II we define some notation and give a summary of the results of our previous paper. In Sec. III we describe the structure of the energy-momentum tensor in Milne coordinates and, by exploiting the symmetries of the tensor,

Published by the American Physical Society under the terms of the Creative Commons Attribution 4.0 International license. Further distribution of this work must maintain attribution to the author(s) and the published article's title, journal citation, and DOI. Funded by SCOAP³.

we give a fairly compact analytic expression for our result to order τ^2 . The order τ^4 results are given in Appendix B. We also formulate a calculation of the angular momentum of the glasma per unit rapidity, on a hypersurface of constant proper time. In Sec. IV we present some numerical results and discuss their significance in the context of heavy-ion collisions at the Relativistic Heavy Ion Collider (RHIC) and the Large Hadron Collider (LHC). In Sec. IV A we define our notation for the geometry of the collision and the units we will use. In Sec. IV B we discuss our method to implement nonconstant nuclear area density functions, which is based on a gradient expansion of a two dimensional projection of a Woods-Saxon distribution. We follow the method of [7] and discuss carefully the limitations of the expansion and how its convergence depends critically on what quantity is calculated. In Secs. IV C and IV D we study the energy density and pressure of the glasma. For a system in equilibrium the transverse and longitudinal pressures are equal to each other, and individually equal to a third of the energy density. A calculation of the pressure therefore gives information about how far the glasma is from equilibrium. We show that, for times small enough that the expansion converges, the transverse and longitudinal pressures move towards their equilibrium values. We calculate a quantity that describes the asymmetry between the transverse and longitudinal pressures, and one that characterizes the difference between the two components of the transverse pressure. We show that the first is almost completely insensitive to the gradient expansion, but the second shows strong dependence. In Sec. IV E we study the flow of the energy of the gluon field by calculating the radial projection of the Poynting vector. Our results in this section, and the previous two sections, indicate that the expansion to order τ^6 can be trusted to about $\tau = 0.05$ fm. In our previous paper [3] we have given a simple argument that this time is much greater than the lower bound at which we no longer trust the classical description that is inherent in our approach. In Sec. IV F we study the momentum anisotropy of the glasma by calculating the Fourier coefficients of the azimuthal distribution of the flow. Anisotropy is an important characteristic because it is primarily sensitive to the properties of the system very early in its evolution. It is expected that the spatial anisotropy of the system that is produced at very early times (within the first few fm) will be encoded in the observed anisotropies of the final particle momentum distributions. Our results for the Fourier coefficients are larger than expected, which does not agree with the common assumption that momentum anisotropy is mostly generated during the hydrodynamic evolution of the plasma. In Sec. IV G we consider the spatial azimuthal asymmetry of the glasma by calculating the eccentricity. We look for correlations between spatial asymmetry and momentum anisotropy, which is characterized by the Fourier coefficients calculated in the previous section. Since momentum anisotropy originates in the initial spatial asymmetries in the geometry of the system, such correlations provide information about the effect of the interactions, and the expansion of the system, during glasma formation. We find significant correlation between the eccentricity and the elliptic flow coefficient calculated in the previous section, which indicates that the spatial asymmetry of the initial energy density is converted

into the anisotropy of the azimuthal distribution of the gluon momentum field, and this correlation is characteristic of hydrolike behavior. In Sec. IV H we look at the angular momentum of the glasma, which develops in collisions with nonzero impact parameter, in the direction perpendicular to the reaction plane. It has been proposed that, because of spin-orbit coupling effects, the angular momentum of the glasma could lead to the polarization of produced quarks and antiquarks, which might be detected by measuring the polarization of the Λ hyperon or various vector mesons [9]. Measurements of this kind could be used to compare different hydrodynamic models and hadronization scenarios [10]. Our results are many orders of magnitude smaller than the initial angular momentum of two ions colliding with nonzero impact parameter. Our findings therefore disagree with the proposal that the glasma acquires a large fraction of the angular momentum of the participating valence quarks [10], but is not contradicted by any experimental evidence, since attempts to measure the polarization of produced hadrons have found only very small effects [11,12]. In Sec. V we conclude with some discussion and comments on possible future directions of this research.

II. SUMMARY OF PREVIOUS WORK

A. Energy-momentum tensor

In a previous paper [3] we calculated the energy-momentum tensor using the CGC effective theory, to sixth order in an expansion in the proper time. In this section, we review the main elements of that calculation.

We consider a collision of two ions moving towards each other along the z axis and colliding at $t = z = 0$. In the precollision region of space-time, the system is most naturally described using light-cone coordinates, but in the postcollision region Milne coordinates are more convenient. At the end of the calculation, when we look at physical quantities, we usually want to use Minkowski coordinates. The calculation is done most efficiently by using the three different coordinate systems at different stages, and transforming between them as needed. We will use greek letters for 4-indices, and latin letters for 2-indices denoting coordinates in the transverse plane. For example, the components of a position 4-vector in Minkowski coordinates (t, z, x, y) are written x^μ with $\mu \in (0, 1, 2, 3)$, and the transverse components are denoted x^i with $i \in (2, 3)$. In light-cone and Milne coordinates, the time and longitudinal coordinates are defined as functions of the Minkowski variables (t, z) , but the transverse coordinates are the same in all three bases. Our notation for light-cone and Milne variables is standard, and is reviewed in Appendix A.

The vector potential of the gluon field is described with the ansatz [13]

$$\begin{aligned} A^+(x) &= \Theta(x^+) \Theta(x^-) x^+ \alpha(\tau, \vec{x}_\perp), \\ A^-(x) &= -\Theta(x^+) \Theta(x^-) x^- \alpha(\tau, \vec{x}_\perp), \\ A^i(x) &= \Theta(x^+) \Theta(x^-) \alpha_\perp^i(\tau, \vec{x}_\perp) + \Theta(-x^+) \Theta(x^-) \\ &\quad \times \beta_1^i(x^-, \vec{x}_\perp) + \Theta(x^+) \Theta(-x^-) \beta_2^i(x^+, \vec{x}_\perp). \end{aligned} \quad (1)$$

The functions $\beta_1^i(x^-, \vec{x}_\perp)$ and $\beta_2^i(x^+, \vec{x}_\perp)$ represent the precollision potentials, and the functions $\alpha(\tau, \vec{x}_\perp)$ and

$\alpha_{\perp}^i(\tau, \vec{x}_{\perp})$ give the postcollision potentials. In the forward light cone the vector potential satisfies the sourceless YM equation. We find solutions valid for early postcollision times by expanding in the proper time τ [4–8]. Using these solutions we can write the postcollision field-strength tensor and energy-momentum tensor in terms of the initial potentials $\alpha(0, \vec{x}_{\perp})$ and $\vec{\alpha}_{\perp}(0, \vec{x}_{\perp})$. The initial potentials are related to the physical properties of the ions and the geometry of the collision using boundary conditions that connect the precollision and postcollision potentials. These conditions are found by integrating the YM equation across the light cone [3,13],

$$\alpha_{\perp}^i(0, \vec{x}_{\perp}) = \alpha_{\perp}^{i(0)}(\vec{x}_{\perp}) = \lim_{w \rightarrow 0} [\beta_1^i(x^-, \vec{x}_{\perp}) + \beta_2^i(x^+, \vec{x}_{\perp})],$$

$$\alpha(0, \vec{x}_{\perp}) = \alpha^{(0)}(\vec{x}_{\perp}) = -\frac{ig}{2} \lim_{w \rightarrow 0} [\beta_1^i(x^-, \vec{x}_{\perp}), \beta_2^i(x^+, \vec{x}_{\perp})], \quad (2)$$

where the notation $\lim_{w \rightarrow 0}$ indicates that the width of the sources across the light cone is taken to zero (the precollision potentials depend only on transverse coordinates in this limit). Using Eqs. (1) and (2) the energy-momentum tensor can be written in terms of the precollision potentials $\vec{\beta}_1(x^-, \vec{x}_{\perp})$ and $\vec{\beta}_2(x^+, \vec{x}_{\perp})$ and their derivatives.

The next step is to use the YM equation to write the precollision potentials in terms of the color charge distributions of the incoming ions. One then averages over a Gaussian distribution of color charges within each nucleus. The average of a product of color charges can be written as a sum of terms that combine the averages of all possible pairs, which is called Wick's theorem. The average of a product of precollision potentials, which depend on the color charges in a nontrivial way, is much more difficult to calculate, and the calculation becomes more and more complicated as the number of potentials increases [14–18]. We use the glasma graph approximation [18], which was also used in other near field expanded calculations, and is equivalent to the application of Wick's theorem to light-cone potentials directly. In our previous work [3] we showed that, for the simple case of homogeneous ions that are infinite in the transverse plane, there is some evidence that the effect of this approximation is small. We stress, however, that the range of validity of the glasma graph approximation has not been carefully studied, and this is an open and important issue.

In the context of our calculation, the use of the glasma graph approximation means that the energy-momentum tensor can be written in terms of the two-point correlators of the precollision potentials. This correlator was originally calculated in Ref. [19] and generalized to include some effects of nuclear structure in Ref. [7]. We give below the result in our notation; see [3] for further details.

The correlator of two potentials from different ions is assumed to be zero. The two-point correlator for two potentials from the same ion is written in terms of the color charge surface density for that ion, which we denote $\mu_1(\vec{x}_{\perp})$ and $\mu_2(\vec{x}_{\perp})$. These functions are not determined by the CGC model; rather, one assumes some form constrained by experimental knowledge. We use a two-dimensional projection of a Woods-Saxon distribution which is characterized by three parameters that

correspond to the surface thickness, radius, and displacement of the center of the ion relative to the beam axis (for details see Sec. II B). The two-point correlators for the two ions have the form

$$\delta^{ab} B_1^{ij}(\vec{x}_{\perp}, \vec{y}_{\perp}) \equiv \lim_{w \rightarrow 0} \langle \beta_{1a}^i(x^-, \vec{x}_{\perp}) \beta_{1b}^j(y^-, \vec{y}_{\perp}) \rangle,$$

$$\delta^{ab} B_2^{ij}(\vec{x}_{\perp}, \vec{y}_{\perp}) \equiv \lim_{w \rightarrow 0} \langle \beta_{2a}^i(x^+, \vec{x}_{\perp}) \beta_{2b}^j(y^+, \vec{y}_{\perp}) \rangle, \quad (3)$$

and using the index $n \in \{1, 2\}$ to represent the two ions we have

$$B_n^{ij}(\vec{x}_{\perp}, \vec{y}_{\perp}) = g^2 \left(\frac{e^{g^4 N_c \Delta \tilde{\gamma}_n(\vec{x}_{\perp}, \vec{y}_{\perp})} - 1}{g^4 N_c \Delta \tilde{\gamma}_n(\vec{x}_{\perp}, \vec{y}_{\perp})} \right) \partial_x^i \partial_y^j \tilde{\gamma}_n(\vec{x}_{\perp}, \vec{y}_{\perp}), \quad (4)$$

where

$$\Delta \tilde{\gamma}_n(\vec{x}_{\perp}, \vec{y}_{\perp}) = \tilde{\gamma}_n(\vec{x}_{\perp}, \vec{y}_{\perp}) - \frac{1}{2} [\tilde{\gamma}_n(\vec{x}_{\perp}, \vec{x}_{\perp}) + \tilde{\gamma}_n(\vec{y}_{\perp}, \vec{y}_{\perp})], \quad (5)$$

$$\tilde{\gamma}_n(\vec{x}_{\perp}, \vec{y}_{\perp}) = \int d^2 z_{\perp} \mu_n(\vec{z}_{\perp}) G(\vec{x}_{\perp} - \vec{z}_{\perp}) G(\vec{y}_{\perp} - \vec{z}_{\perp}), \quad (6)$$

$$G(\vec{x}_{\perp}) = \frac{1}{2\pi} K_0(m|\vec{x}_{\perp}|). \quad (7)$$

The function K_0 is a modified Bessel function of the second kind, and m is an infrared regulator. In the limit $m \rightarrow 0$ the Green's function $G(\vec{x}_{\perp})$ goes like $\sim \ln(m|\vec{x}_{\perp}|)$. Since valence parton sources come from individual nucleons, the Green's function should go to zero when $|\vec{x}_{\perp}|$ approaches the confinement scale, and therefore we choose $m \sim \Lambda_{\text{QCD}}$.

B. Parton surface density

To make further progress we must specify the form of the color charge surface density of the nuclei. We will use a two-dimensional projection of a Woods-Saxon potential of the form

$$\mu(\vec{x}_{\perp}) = \left(\frac{A}{207} \right)^{1/3} \frac{\bar{\mu}}{2a \ln(1 + e^{R_A/a})} \times \int_{-\infty}^{\infty} dz \frac{1}{1 + \exp[(\sqrt{(\vec{x}_{\perp})^2 + z^2} - R_A)/a]}. \quad (8)$$

The parameters R_A and a give the radius and skin thickness of a nucleus of mass number A , and their numerical values are discussed in Sec. IV B. The integral in (8) is normalized so that for a lead nucleus $\mu(\vec{0}) = \bar{\mu}$, which is sometimes called the McLerran-Venugopalan (MV) scale. This parameter is related to the saturation scale Q_s , but its exact value cannot be determined within the CGC approach (for a discussion see [20]). We use $\bar{\mu} = Q_s^2/g^4$, and some motivation for this choice can be found in [3]. Due to the ambiguity associated with the value of the MV scale, our numerical results for quantities like the energy density and pressure should be regarded as order-of-magnitude estimates. Quantities that depend on ratios of different elements of the energy momentum tensor, like Fourier coefficients of the azimuthal flow, will have much weaker dependence on the MV scale.

We obtain an analytic result for the energy-momentum tensor by substituting Eq. (8) into Eq. (6) and performing a

gradient expansion, using the method developed in Ref. [7]. The coordinates \vec{x}_\perp and \vec{y}_\perp are rewritten in terms of relative and average coordinates. To consider collisions with nonzero impact parameter we expand the distribution $\mu_1(\vec{z}_\perp)$ around the average coordinate $(\vec{x}_\perp + \vec{y}_\perp)/2 = \vec{R} - \vec{b}/2$, and $\mu_2(\vec{z}_\perp)$ around $(\vec{x}_\perp + \vec{y}_\perp)/2 = \vec{R} + \vec{b}/2$. We will keep terms up to second order in gradients of the distribution. The parameter that we assume to be small is

$$\delta = \frac{|\nabla^i \mu(\vec{R} \pm \frac{\vec{b}}{2})|}{m\mu(\vec{R} \pm \frac{\vec{b}}{2})}, \quad (9)$$

where the gradient operator indicates differentiation with respect to the argument of the function. The region of validity of this expansion is discussed in Sec. IV B.

We remind the reader that for a realistic nucleus, which is made up of individual partons, the transverse charge distribution is not a very smooth function. It is possible that the transverse charge distribution of a real nucleus could be sufficiently irregular that a Woods-Saxon distribution is not a good representation.

C. Two-particle correlators

In this subsection we drop the subscript that indicates which ion is being considered, and we set $\vec{b} = 0$. Performing the derivative expansion and keeping terms up to second order in gradients of μ , Eq. (6) becomes

$$\begin{aligned} \tilde{\gamma}(\vec{x}_\perp, \vec{y}_\perp) &= \frac{\mu(\vec{R})r}{4\pi m} K_1(mr) + \frac{1}{2} \nabla^i \nabla^j \mu(\vec{R}) \\ &\times \left(\delta^{ij} \frac{r^2}{24\pi m^2} K_2(mr) + \frac{r^i r^j}{r^2} \frac{r^3}{48\pi m} K_1(mr) \right). \end{aligned} \quad (10)$$

We can rewrite equation (10) in the form

$$\begin{aligned} \tilde{\gamma}(\vec{x}_\perp, \vec{y}_\perp) &= \mu(\vec{R}) \int \frac{d^2 k}{(2\pi)^2} \frac{e^{i\vec{r}\cdot\vec{k}}}{(k^2 + m^2)^2} \\ &+ \frac{m^2}{2} \nabla^2 \mu(\vec{R}) \int \frac{d^2 k}{(2\pi)^2} \frac{e^{i\vec{r}\cdot\vec{k}}}{(k^2 + m^2)^4}, \end{aligned} \quad (11)$$

where we have made the replacement $\hat{r}^i \hat{r}^j \rightarrow \delta^{ij}/2$, because in the limit $\vec{r} \rightarrow 0$ we know $\tilde{\gamma}$ must be independent of the direction of the vector \hat{r} . We note we are able to make this replacement before performing any derivatives with respect to \vec{x}_\perp and \vec{y}_\perp , since $\lim_{r \rightarrow 0} \partial_x^i \dots \partial_y^j \dots \hat{r}^k \hat{r}^l = 0$, where the dots indicate any number of derivatives.

The correlator $B^{ij}(\vec{x}_\perp, \vec{y}_\perp)$ and its derivatives have ultraviolet divergences that must be regulated. We use a modified version of the method proposed in Ref. [6]. To illustrate how we make use of Eq. (11) we consider, for example, the calculation of

$$\begin{aligned} \partial_x^i \partial_y^j \tilde{\gamma}(\vec{x}_\perp, \vec{y}_\perp) &= \mu(\vec{R}) \int \frac{d^2 k}{(2\pi)^2} \frac{k^i k^j e^{i\vec{r}\cdot\vec{k}}}{(k^2 + m^2)^2} \\ &+ \frac{m^2}{2} \nabla^2 \mu(\vec{R}) \int \frac{d^2 k}{(2\pi)^2} \frac{k^i k^j e^{i\vec{r}\cdot\vec{k}}}{(k^2 + m^2)^4}, \end{aligned} \quad (12)$$

which appears in the expression for B^{ij} in Eq. (4). The integration over angular variables gives $k^i k^j \rightarrow \delta^{ij} k^2/2$. The second term in (12) is finite, but the first term is logarithmically divergent and we regulate it using an ultraviolet momentum cutoff Λ . This cutoff will be set to the saturation scale; see our previous paper [3] for some discussion of this point. In Sec. IV D 1 we test the dependence of some of our results on the saturation scale, and show that they are not very sensitive to its numerical value.

Now we consider the contribution from the factor in round brackets in equation (4). Expanding this factor we have

$$\begin{aligned} \frac{e^{g^4 N_c \Delta \tilde{\gamma}_n(\vec{x}_\perp, \vec{y}_\perp)} - 1}{g^4 N_c \Delta \tilde{\gamma}_n(\vec{x}_\perp, \vec{y}_\perp)} &= 1 + \frac{1}{2} g^4 N_c \Delta \tilde{\gamma}(\vec{x}_\perp, \vec{y}_\perp) \\ &+ \frac{1}{6} [g^4 N_c \Delta \tilde{\gamma}(\vec{x}_\perp, \vec{y}_\perp)]^2 + \dots \end{aligned} \quad (13)$$

When we calculate derivatives of the correlator $B^{ij}(\vec{x}_\perp, \vec{y}_\perp)$, the derivatives operate on all terms in the expansion in Eq. (13). At sixth order in the τ expansion the energy-momentum tensor includes terms with six derivatives acting on the correlator in Eq. (4). Naively it would seem that we need to expand the exponent in Eq. (13) to seventh order, since each of the six derivative operators will have a piece proportional to $\partial/\partial r^i$ which could act separately on each of the six factors in the term $[\Delta \tilde{\gamma}(\vec{x}_\perp, \vec{y}_\perp)]^6$. For example, if we differentiate six times with respect to r^1 we obtain an expression of the form

$$\lim_{\vec{r} \rightarrow 0} \left(\frac{\partial}{\partial r^1} \right)^6 [\Delta \tilde{\gamma}(\vec{x}_\perp, \vec{y}_\perp)]^6 = \lim_{\vec{r} \rightarrow 0} \left(\frac{\partial}{\partial r^1} \tilde{\gamma}(\vec{x}_\perp, \vec{y}_\perp) \right)^6 + \dots, \quad (14)$$

where the dots represent additional terms that give zero when \vec{r} is taken to zero. However, it is easy to see from Eq. (11) that if we differentiate $\tilde{\gamma}$ an odd number of times with respect to r^1 or r^2 , the integration over momentum variables gives zero. This means terms with more than three factors of $\Delta \tilde{\gamma}$, which are operated on with a maximum of six derivatives with respect to components of \vec{r} , can be set to zero. Equivalently, we have to expand the exponential only to fourth order.

All correlators and their derivatives can be obtained using the method described above. We give one example:

$$\begin{aligned} \lim_{r \rightarrow 0} B^{ij}(\vec{x}_\perp, \vec{y}_\perp) &= \delta^{ij} g^2 \frac{\mu(\vec{R})}{8\pi} \left[\ln \left(\frac{\Lambda^2}{m^2} + 1 \right) - \frac{\Lambda^2}{\Lambda^2 + m^2} \right] \\ &+ \frac{g^2}{16\pi(\Lambda^2 + m^2)} \left[\delta^{ij} \nabla^2 \mu(\vec{R}) \frac{\Lambda^4}{6m^2(\Lambda^2 + m^2)} \right. \\ &\times \left. \left(1 + \frac{2m^2}{\Lambda^2 + m^2} \right) + \nabla^i \nabla^j \mu(\vec{R}) \frac{\Lambda^2}{m^2} \right]. \end{aligned} \quad (15)$$

III. ANALYTIC RESULTS

A. Structure of the energy-momentum tensor

In this section we present our analytic result for the energy-momentum tensor, to order τ^6 . For simplicity of notation we

give our results for the tensor in Milne coordinates, where there is no dependence on rapidity. All elements in the energy-

momentum tensor have either even or odd powers of τ . We summarize this information in the symbolic equation

$$\mathcal{O}(T_{\text{milne}}) = \begin{pmatrix} (0, 2, 4, 6) & (1, 3, 5) & (1, 3, 5) & (1, 3, 5) \\ (1, 3, 5) & (-2, 0, 2, 4) & (0, 2, 4) & (0, 2, 4) \\ (1, 3, 5) & (0, 2, 4) & (0, 2, 4, 6) & (2, 4, 6) \\ (1, 3, 5) & (0, 2, 4) & (2, 4, 6) & (0, 2, 4, 6) \end{pmatrix}. \quad (16)$$

The top left element of the tensor shows that the element T^{00} has contributions of order τ^0 , τ^2 , τ^4 , and τ^6 . To give one other example, the entry in the top right corner shows that the element T^{03} has contributions of order τ , τ^3 , and τ^5 .

We do not need to give all components of the energy-momentum tensor because of its symmetry properties. We will give our results for the six elements in Eq. (17) that are written in boldface. All of the other elements in the tensor can be generated from these using symmetries, as explained below. We emphasize that we have calculated all elements of the energy-momentum tensor, and the symmetries summarized in Eq. (17) have been verified, and not assumed.

All elements below the diagonal can be related to elements above the diagonal using the fact that the tensor is symmetric. In Eq. (17) we write, for example, $T^{10} = T^{01}$. There are also pairs of elements where one can be obtained from the other using the transformation $\nabla_x \leftrightarrow \nabla_y$, where we have defined $\nabla_x \equiv \partial/\partial R^x$ and $\nabla_y \equiv \partial/\partial R^y$. We will also use $\nabla^2 \equiv \nabla_x^2 + \nabla_y^2$. For example, we write $T^{13} = \mathcal{F}T^{12}$ to indicate that the element T^{13} can be obtained from T^{12} by interchanging the derivative operators ∇_x and ∇_y . Finally, since the energy-momentum

tensor is traceless it satisfies $g_{\mu\nu}T^{\mu\nu} = 0$, which means that we do not have to give all elements on the diagonal. We replace the element T^{11} with the symbol Tr to indicate that this matrix element can be constructed from the other diagonal elements of the tensor. Combining this information we write

$$T_{\text{milne}} \longrightarrow \begin{pmatrix} \mathbf{T}^{00} & \mathbf{T}^{01} & \mathbf{T}^{02} & \mathcal{F}T^{02} \\ T^{01} & \text{Tr} & \mathbf{T}^{12} & \mathcal{F}T^{12} \\ T^{02} & T^{12} & \mathbf{T}^{22} & \mathbf{T}^{23} \\ T^{03} & T^{13} & T^{23} & \mathcal{F}T^{22} \end{pmatrix}. \quad (17)$$

In summary, Eq. (17) tells us that we need to give only the six elements of the energy-momentum tensor that are written in boldface.

B. Coefficients of the energy-momentum tensor

We give generic equations for these elements organized by powers of τ and numbers of derivatives with respect to each of the transverse coordinates. Our result for the energy-momentum tensor has the form

$$\begin{aligned} T^{00} &= \mathcal{E}_0^{00} + (1 + \mathcal{F})\mathcal{E}_0^{02} + \tau^2(\frac{1}{6}\nabla^2\mathcal{E}_0^{00} + \mathcal{E}_2^{00} + (1 + \mathcal{F})\mathcal{E}_2^{20}) + \tau^4(\frac{1}{10}\nabla^2\mathcal{E}_2^{00} + \mathcal{E}_4^{00} + (1 + \mathcal{F})\mathcal{E}_4^{02}) + \tau^6[\mathcal{E}_6^{00} + (1 + \mathcal{F})\mathcal{E}_6^{02}], \\ T^{01} &= -\frac{1}{8}(1 + \mathcal{F})(2\tau\nabla_x\beta_0^{10} + \frac{4}{3}\tau^3\nabla_x\beta_2^{10} + \tau^5\nabla_x\beta_4^{10}), \\ T^{02} &= -\frac{1}{2}\tau\nabla_x\mathcal{E}_0^{00} - \frac{1}{2}\tau^3\nabla_x\mathcal{E}_2^{00} - \frac{1}{2}\tau^5\nabla_x\mathcal{E}_4^{00}, \\ T^{12} &= \beta_0^{10} + \tau^2\beta_2^{10} + \tau^4\beta_4^{10}, \\ T^{22} &= \mathcal{E}_0^{00} + (1 + \mathcal{F})\mathcal{E}_0^{02} + \tau^2(2\mathcal{E}_2^{00} + \delta_2^{20} + \delta_2^{02}) + \tau^4(3\mathcal{E}_4^{00} + \delta_4^{20} + \delta_4^{02}) + \tau^6(4\mathcal{E}_6^{00} + \delta_6^{20} + \delta_6^{02}), \\ T^{23} &= \tau^2\gamma_2^{11} + \tau^4\gamma_4^{11} + \tau^6\gamma_6^{11}. \end{aligned} \quad (18)$$

For each of the greek letter variables in Eq. (18) the subscript gives power of τ that multiplies the variable when it is not acted on by any external derivatives, and the superscripts give the number of internal derivatives with respect to R_x and R_y . For example, the second term in T^{12} contains the variable β_2^{10} which has coefficient τ^2 and is defined [see Eq. (20)] as a sum of terms each of which has one derivative with respect to R_x .

We use \mathcal{X} to denote any of the greek letters $\{\mathcal{E}, \beta, \gamma, \delta, \xi\}$. We give below our results for \mathcal{X}_n^{lm} with $0 \leq n \leq 2$. In Appendix B we give our results for \mathcal{X}_n^{lm} with $n = 4$. Each symbol is either even or odd under the transformation $\mu_1 \leftrightarrow \mu_2$, and therefore we only need to give half of the terms, and the sign of the symmetry. We set the ultraviolet cutoff Λ

equal to the saturation scale Q_s and introduce the notation $L \equiv \ln(Q_s/m)$. To save space we give only the contributions that are leading order in an expansion in the infrared mass m , and this power counting is done with the assumption $(\nabla_x)^{n_i}(\nabla_y)^{n_j}\mu_1(\vec{R})/\mu_1(\vec{R}) \sim m^{n_i+n_j}$ [and similarly for $\mu_2(\vec{R})$]. We will also factor the constant $\bar{\mu} \equiv Q_s^2/g^4$ out of the source density functions and define $\hat{\mu}_1(\vec{R}) \equiv \mu_1(\vec{R})/\bar{\mu}$, and similarly for ion 2. To save space we will use the shorthand notation $\hat{\mu}_1^{10} \equiv \nabla_x\hat{\mu}_1(\vec{R})$, $\hat{\mu}_1^{11} \equiv \nabla_x\nabla_y\hat{\mu}_1(\vec{R})$, etc. We emphasize that in all of our numerical calculations there is no expansion in m , and we include all contributions from the gradient expansion up to second order.

Using the notation defined above, the coefficients of the energy-momentum tensor at order τ^0 have the simple form

$$\begin{aligned}\mathcal{E}_0^{00} &= \frac{3\hat{\mu}_1\hat{\mu}_2Q_s^4}{8\pi^2g^2}(2L-1)^2 + (\hat{\mu}_1 \leftrightarrow \hat{\mu}_2), \\ \beta_0^{10} &= \frac{3\hat{\mu}_1Q_s^4\hat{\mu}_2^{10}}{8\pi^2g^2}(2L-1)^2 - (\hat{\mu}_1 \leftrightarrow \hat{\mu}_2), \\ \mathcal{E}_0^{02} &= \frac{\hat{\mu}_1Q_s^4\hat{\mu}_2^{02}}{4\pi^2g^2m^2}(2L-1) + (\hat{\mu}_1 \leftrightarrow \hat{\mu}_2).\end{aligned}\quad (19)$$

At order τ^2 we have

$$\begin{aligned}\beta_2^{10} &= \frac{27\hat{\mu}_1Q_s^6}{512\pi^3g^2}((2L-1)\{11\hat{\mu}_2(1-2L)^2\hat{\mu}_1^{10} \\ &\quad + [11\hat{\mu}_1(1-2L)^2 - 8\pi]\hat{\mu}_2^{10}\}) - (\hat{\mu}_1 \leftrightarrow \hat{\mu}_2), \\ \gamma_2^{11} &= \frac{9\hat{\mu}_1Q_s^6}{512\pi^3g^2m^2}((1-2L)^2(8\hat{\mu}_2\hat{\mu}_1^{11} \\ &\quad + 7\hat{\mu}_1\hat{\mu}_2^{11})) + (\hat{\mu}_1 \leftrightarrow \hat{\mu}_2), \\ \delta_2^{02} &= -\frac{\hat{\mu}_1Q_s^6}{1024\pi^3g^2m^2}(750\hat{\mu}_2(2L-1)^2\hat{\mu}_1^{02} \\ &\quad + [447\hat{\mu}_1(2L-1)^2 + 128\pi]\hat{\mu}_2^{02}) + (\hat{\mu}_1 \leftrightarrow \hat{\mu}_2), \\ \delta_2^{20} &= -\frac{\hat{\mu}_1Q_s^6}{1024\pi^3g^2m^2}(606\hat{\mu}_2(1-2L)^2\hat{\mu}_1^{20} \\ &\quad + [321\hat{\mu}_1(1-2L)^2 + 128\pi]\hat{\mu}_2^{20}) + (\hat{\mu}_1 \leftrightarrow \hat{\mu}_2), \\ \mathcal{E}_2^{00} &= -\frac{3\hat{\mu}_1\hat{\mu}_2(2L-1)Q_s^6}{16\pi^3g^2}(3\hat{\mu}_2(2L-1)^2 + \pi) \\ &\quad + (\hat{\mu}_1 \leftrightarrow \hat{\mu}_2), \\ \mathcal{E}_2^{02} &= -\frac{\hat{\mu}_1Q_s^6}{1024\pi^3g^2m^2}(339\hat{\mu}_2(2L-1)^2\hat{\mu}_1^{02} \\ &\quad + 64[3\hat{\mu}_1(2L-1)^2 + \pi]\hat{\mu}_2^{02}) + (\hat{\mu}_1 \leftrightarrow \hat{\mu}_2).\end{aligned}\quad (20)$$

C. Angular momentum

In this section we derive an expression for the angular momentum of the glasma per unit rapidity. Our method is similar to that of Ref. [8]. We define the tensor

$$M^{\mu\nu\lambda} = T^{\mu\nu}R^\lambda - T^{\mu\lambda}R^\nu, \quad (21)$$

where R^μ denotes a component of the position vector (τ, η, \vec{R}) . The energy momentum tensor is divergenceless, and therefore the tensor in Eq. (21) satisfies the tensor equation $\nabla_\mu M^{\mu\nu\lambda} = 0$. Using Stokes' theorem one obtains a set of six conserved quantities,

$$J^{\nu\lambda} = \int_\Sigma d^3y \sqrt{|\gamma|} n_\mu M^{\mu\nu\lambda}, \quad (22)$$

where n^μ is a unit vector perpendicular to the hypersurface Σ , γ is the induced metric on this hypersurface, and d^3y is the corresponding volume element. The angular momentum is obtained from the Pauli-Lubanski vector

$$L_\mu = -\frac{1}{2}\epsilon_{\mu\alpha\beta\gamma}J^{\alpha\beta}u^\gamma, \quad (23)$$

where u^ν is the vector that denotes the rest frame of the system. One can easily verify that Eqs. (21)–(23) reduce to the usual definition of angular momentum in Minkowski space. We denote indices for spatial variables in Minkowski space with underscored latin letters, for example $\underline{i} \in (1, 2, 3)$ and $x^{\underline{i}}$ is a component of the vector (x, y, z) . We use $n^\mu = (1, 0, 0, 0)$ so that Σ is a hypersurface of constant t , and with $u^\nu = (1, 0, 0, 0)$ Eq. (23) becomes

$$\begin{aligned}L_{\text{mink}}^{\underline{i}} &= -\frac{1}{2}\epsilon^{\underline{i}jk}J^{\underline{j}k} = -\frac{1}{2}\epsilon^{\underline{i}jk} \int d^3\vec{x} (T^{0\underline{j}}x^{\underline{k}} - T^{0\underline{k}}x^{\underline{j}}) \\ &= \epsilon^{\underline{i}jk} \int d^3\vec{x} x^{\underline{j}}P^{\underline{k}},\end{aligned}\quad (24)$$

where $d^3\vec{x}$ represents the spatial volume element in Minkowski space, and we have written the Poynting vector $P^i \equiv T^{0i}$.

We work in Milne coordinates and use $n^\mu = (1, 0, 0, 0)$ so that

$$J^{\nu\lambda} = \tau \int d\eta d^2\vec{R} M^{0\nu\lambda} \quad (25)$$

is defined on a hypersurface of constant τ . Using $u^\nu = (1, 0, 0, 0)$ gives

$$L_\mu = \frac{1}{2}\tau \epsilon_{0\mu\alpha\beta} \int d\eta \int d^2\vec{R} (T^{0\alpha}R^\beta - T^{0\beta}R^\alpha). \quad (26)$$

In our calculation angular momentum is not conserved, because the currents on the light cone act as sources, and therefore we consider instead the angular momentum per unit rapidity. From Eq. (26) we obtain¹

$$\frac{dL_\mu}{d\eta} = \frac{1}{2}\tau \epsilon_{0\mu\alpha\beta} \int d^2\vec{R} (T^{0\alpha}R^\beta - T^{0\beta}R^\alpha). \quad (27)$$

We note that, although the right side of Eq. (27) is independent of rapidity, our calculation is only meaningful close to midrapidity where boost invariance is a good approximation.

The integral over the transverse plane in Eq. (27) can be simplified using symmetry considerations. The source charge distributions that we use (see Sec. II B) are even under the transformation $R^y \rightarrow -R^y$. We will consider symmetric displacements of the ions relative to the collision axis ($\vec{b}_1 = -\vec{b}_2$) so that the transformation $R^x \rightarrow -R^x$ interchanges the distributions for the first and second ions. Using these symmetries one can show that each component of the energy momentum tensor in Milne coordinates is either even or odd under the R^x and R^y parity transformations. We summarize these symmetries in Table I. Using the symmetry relation in Table I it is easy to see that the only non-zero component of the angular momentum per unit rapidity is

$$\frac{dL^y}{d\eta} = -\tau^2 \int d^2\vec{R} R^x T^{01}. \quad (28)$$

¹We comment that our result is different from that of Ref. [8], where a slightly inconsistent procedure is used. In that paper the authors define angular momentum in Minkowski space, on a surface of constant time, and then enforce separately that the integral should be calculated with τ held fixed.

TABLE I. Symmetries of the components of the energy-momentum tensor under the transformations $R_x \rightarrow -R_x$ and $R_y \rightarrow -R_y$.

	$R_x \rightarrow -R_x$	$R_y \rightarrow -R_y$
T^{00}	even	even
T^{01}	odd	even
T^{02}	odd	even
T^{03}	even	odd
T^{11}	even	even
T^{12}	even	even
T^{13}	odd	odd
T^{22}	even	even
T^{23}	odd	odd
T^{33}	even	even

IV. NUMERICAL RESULTS

A. Notation and units

We remind the reader of the geometry of the collision we are considering. The two ions approach each other along the z axis and collide at the origin, at time $t = 0$. Post collision, the first ion moves outward along the positive z axis and the second ion moves along the negative z axis. We will consider collisions with nonzero impact parameter, which we denote b . The displacement vector for the first ion is $\vec{b}_1 = (b/2, 0)$ and for the second ion we use $\vec{b}_2 = (-b/2, 0)$. Energy and pressure are given in GeV and lengths in fm (we use natural units $c = \hbar = 1$). We define a dimensionless time variable $\tilde{\tau} = \tau Q_s$. We use $N_c = 3$, $m = 0.2$ GeV, $Q_s = 2$ GeV, and $g = 1$, unless stated otherwise. We consider lead-lead collisions, which corresponds to mass numbers $A_1 = A_2 = 207$, except for a few situations where we will explicitly specify different mass numbers. We will show below that our results to order τ^6 are valid to $\tau \approx 0.05$ fm, which corresponds to $\tilde{\tau} \approx 0.51$.

B. Physical observables and the gradient expansion

The form of the charge density function $\mu(\vec{x}_\perp)$ that we use is discussed in Sec. II B. We use $r_0 = 1.25$ fm and $a = 0.5$ fm so that the radius of a nucleus with $A = 207$ is $R_A = r_0 A^{1/3} = 7.4$ fm. As explained in Sec. II B, we allow for nonhomogeneous nuclear density functions by performing a gradient expansion around the coordinate that gives the position of the center of each nucleus in the transverse plane. In Fig. 1 we show the density function with $\vec{x}_\perp = (R_x, 0)$, its first and second derivatives with respect to R_x , and the quantity δ in Eq. (9) which must be small for the gradient expansion to converge. The condition $\delta < 0.75$ is satisfied in the region to the left of the vertical line in the figure. Figure 1 shows clearly that the derivatives of the density function are appreciable only in a very small region at the edges of the nucleus. This means that if we calculate a quantity for which the dominant part of the integrand is not close to the edges of the nuclei, the gradient expansion will converge well, but the contributions of the derivative terms will likely be so small that they are negligible. On the other hand, if we calculate a quantity for which the

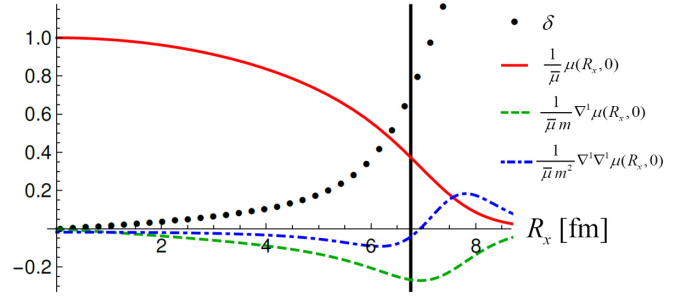


FIG. 1. The red (solid), green (dashed), and blue (dot-dashed) curves show the density function and its first and second derivatives. The quantity δ in Eq. (9) is shown by the black dots. For illustration the figure shows a vertical line that indicates the value of R_x for which $\delta = 0.75$.

region of the transverse plane close to the edges of the nuclei is important, the contribution from the derivative terms can be large, but the convergence of the gradient expansion must be studied carefully.

In Sec. IV C we look at the energy density of the glasma. We restrict to the region of the transverse plane for which $-5 \text{ fm} < |\vec{R}| < 5 \text{ fm}$. The corresponding condition on the expansion parameter is $\delta \lesssim 0.2$, and the gradient expansion converges well. Within this region, the inhomogeneity of the energy density in the transverse plane is almost entirely due to the asymmetry created by a nonzero impact parameter, which produces an almond shaped region of overlap. The gradients of the individual charge distributions are small and mostly irrelevant. In Sec. IV D we calculate the pressure of the glasma. To illustrate the issues associated with the gradient expansion we look at two different quantities, one of which describes the asymmetry between the transverse and longitudinal pressures, and the other characterizes the difference between the two components of the transverse pressure. We show that the former is almost completely insensitive to the gradient expansion, whereas the latter depends strongly on the behavior of the nuclear density function $\mu(\vec{x}_\perp)$ close to the nuclear radii. In Sec. IV E we look at various projections of the Poynting vector which describes the flow of the energy of the gluon field. The leading-order contribution to the Poynting vector comes solely from the first-order term in the gradient expansion, which means that we can restrict to the region where the expansion parameter δ is small, and still see clearly the contribution of the gradient terms. In Sec. IV F we study the momentum anisotropy of the glasma by calculating the Fourier coefficients of the azimuthal distribution of the flow, and in Sec. IV G we look at the spatial azimuthal asymmetry of the glasma by calculating the eccentricity. These calculations involve integration over the transverse plane, and are therefore potentially sensitive to the gradient expansion. One must show that results are largely insensitive to the choice of the integration limits, and we will find that this condition restricts us to the consideration of small impact parameters. This is because when the centers of the two ions are separated, the inner edge of the first (second) ion, where the density changes rapidly, will be closer to the center of the second (first) ion, where integrand can be large. In Sec. IV H we

TABLE II. Configurations of colliding ions.

	<i>A</i>	<i>B</i>	<i>C</i>	<i>D</i>
A_1	207	207	207	207
A_2	207	207	40	40
$b_{1/2}$	0	3	3	0
$b_{2/2}$	0	-3	-3	0
\mathcal{E}_0^{\max} GeV/fm ³	2080	1715	722	1202

look at the angular momentum of the glasma. In this case the gradient expansion severely limits the accuracy of the calculation, but we are able to see that the angular momentum carried by the glasma is many orders of magnitude smaller than the total angular momentum of the participant nucleons of the colliding nuclei [21,22].

C. Energy density

We look at the initial energy density $\mathcal{E} = T_{\text{mink}}^{00}$ at mid-spatial-rapidity ($\eta = 0$) for four different configurations of the colliding ions which are defined in Table II. The last row of the table shows the maximum initial energy density. In Fig. 2 we show, for case *B*, the initial energy density, and the difference between the energy density at $\tilde{\tau} = 0.42$ and the initial energy density. The energy density drops fastest at the center and more slowly at the edges of the almond shaped interaction region.

D. Pressures

1. Transverse and longitudinal pressures

We define the normalized longitudinal and transverse pressures as

$$\frac{p_L}{\mathcal{E}} = \frac{T_{\text{mink}}^{11}}{T_{\text{mink}}^{00}} \quad \text{and} \quad \frac{p_T}{\mathcal{E}} = \frac{1}{2} \frac{(T_{\text{mink}}^{22} + T_{\text{mink}}^{33})}{T_{\text{mink}}^{00}}. \quad (29)$$

For a system in equilibrium $p_T/\mathcal{E} = p_L/\mathcal{E} = 1/3$. The glasma energy-momentum tensor at $\tau = 0^+$ has the diagonal form

(with both indices raised)

$$T_{\text{mink}}^{\text{initial}} = \begin{pmatrix} \mathcal{E}_0 & 0 & 0 & 0 \\ 0 & -\mathcal{E}_0 & 0 & 0 \\ 0 & 0 & \mathcal{E}_0 & 0 \\ 0 & 0 & 0 & \mathcal{E}_0 \end{pmatrix}. \quad (30)$$

We remind the reader that in our notation the components of a position 4-vector in Minkowski coordinates are (t, z, x, y) . Equation (30) shows that the initial longitudinal pressure is large and negative. The initial system is therefore not only far from equilibrium, but also far from the regime where a quasi-particle picture would be valid. As τ increases the longitudinal pressure grows and, because the energy-momentum tensor is traceless, the transverse pressure decreases.

In Fig. 3 we show the vector $(p_L/\mathcal{E}, p_T/\mathcal{E})$ in the transverse plane with $b = \eta = 0$. In the left panel we see $-p_L = p_T$ at $\tau = 0$. In the next two panels we use the biggest value of τ for which we trust the τ expansion at that order (these times are determined from additional results in this and the following sections; see for example Figs. 4 and 10). In the middle figure we include terms to order τ^4 and set $\tau = 0.04$ fm. The figure shows that the vector has straightened slightly across the transverse plane. In the right figure we include all terms to order τ^6 and use $\tau = 0.052$ fm. We see that the vector has straightened even more, but not uniformly.

The authors of Ref. [23] suggested that the anisotropy of the transverse and longitudinal pressures should be characterized using the quantity

$$A_{TL} \equiv \frac{3(p_T - p_L)}{2p_T + p_L}, \quad (31)$$

which takes the value $A_{TL} = 6$ at $\tau = 0$ [using Eq. (30)] and would be zero in an equilibrated isotropic plasma. We expect that A_{TL} should decrease as τ increases, up until the point at which the proper time expansion breaks down. This behavior is observed in Fig. 4 which shows A_{TL} versus $\tilde{\tau}$ at three different orders in the τ expansion. The three curves are very close to each other up to about $\tilde{\tau} = 0.2$, and the fourth- and sixth-order expansions agree well up to about $\tilde{\tau} = 0.4$. In Sec. IV E we show additional evidence that the sixth-order expansion can be trusted to about $\tilde{\tau} = 0.5$. We note that for the simpler case of nuclei that are uniform in the transverse plane resummations of selected sets of terms have been used to

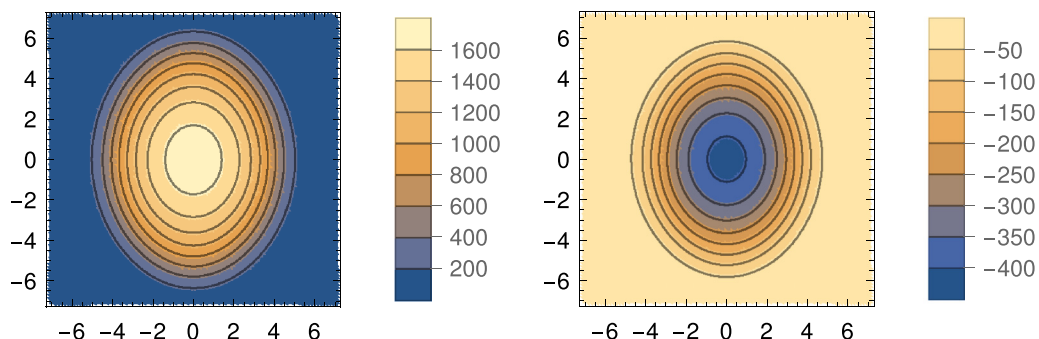


FIG. 2. Energy densities in the transverse plane for case *B*. The left panel shows the energy density at $\tilde{\tau} = 0$ and the right panel shows the difference between the energy density at $\tilde{\tau} = 0.42$ and the initial energy density. The units are GeV/fm³ and the axes show R_x and R_y in fm.

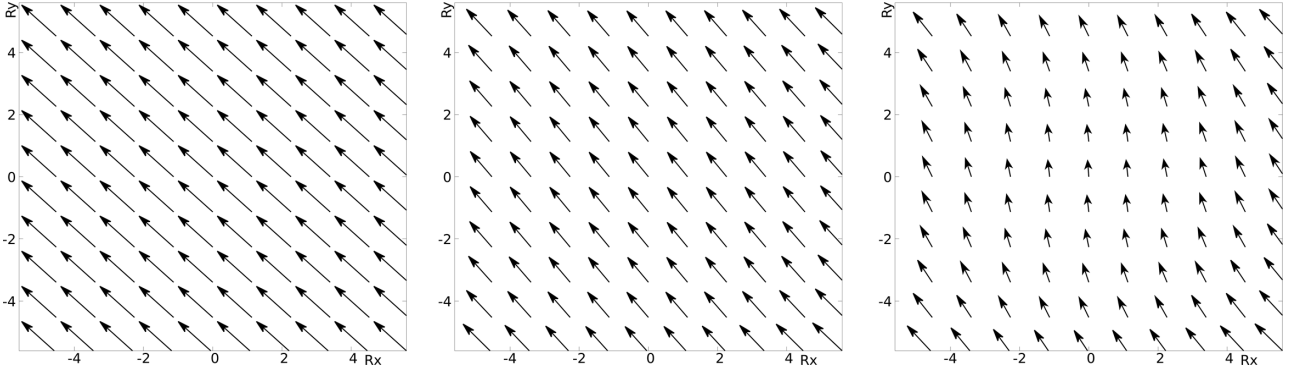


FIG. 3. The vector $(p_L/\mathcal{E}, p_T/\mathcal{E})$ with $b = \eta = 0$ at $\tau = 0$ (left), $\tau = 0.04$ fm to order τ^4 (middle), and $\tau = 0.052$ fm to order τ^6 (right). The axes show R_x and R_y in fm.

increase the range of convergence of the energy and pressure [3,5,24].

We also study how the behavior of A_{TL} depends on azimuthal angle (denoted ϕ), spatial rapidity, and impact parameter. As expected, A_{TL} moves towards the equilibrium value more quickly when the impact parameter is smaller, and the region where the two ions overlap is greater. In Fig. 5 we show the quantity A_{TL} at sixth order in the proper time expansion as a function of $\tilde{\tau}$, for different values of η and ϕ . We consider $\phi = 0$, which corresponds to \vec{R} in the reaction plane, and $\phi = \pi/2$, where \vec{R} is perpendicular to the reaction plane. The graph shows that A_{TL} drops more quickly when either the azimuthal angle or the spatial rapidity increases.

In Fig. 6 we show contour plots of A_{TL} in the transverse plane for $\eta = 0$, $b = 0$, and $\tau = 0.045$ fm at order τ^4 and τ^6 . One sees that when the order τ^6 terms are included, the region of the transverse plane where A_{TL} is small is significantly broader.

In Fig. 7 we show contour plots of A_{TL} in the transverse plane for $\eta = 0$, $b = 0$ at order τ^6 for three different times. One sees that the value of A_{TL} shrinks across the transverse plane as τ increases.

We can also use the quantity A_{TL} to demonstrate that our results are not strongly dependent on the UV and IR scales that enter the calculation (Q_s and m in our notation). This is important because the exact values of these scales are not

known, and also because the way that these scales enter the calculation depends on the method chosen to perform the regularization. In all calculations in this paper we have used $Q_s = 2.0$ GeV and $m = 0.2$ GeV. In Fig. 8 we show A_{TL} at order τ^6 as a function of time for three different values of Q_s with $m = 0.2$ GeV (left panel) and for three different values of m with $Q_s = 2.0$ GeV (right panel). The graphs show that, within the range of validity of the τ expansion, the dependence on the value of these scales is weak.

2. Transverse pressure anisotropy

In this section we look at a quantity that can be used to characterize the asymmetry of the transverse pressure. We define [25]

$$\{A_{xy}\} \equiv \frac{\langle T^{yy} - T^{xx} \rangle}{\langle T^{xx} + T^{yy} \rangle}, \quad (32)$$

where the angular brackets indicate integration over the transverse plane. For comparison we will also calculate

$$\{A_{TL}\} \equiv \frac{3\langle p_T - p_L \rangle}{\langle 2p_T + p_L \rangle}. \quad (33)$$

The leading-order contribution to $\{A_{xy}\}$ comes from the first-order term in the gradient expansion, and therefore this quantity, in contrast to $\{A_{TL}\}$, will be sensitive to the region of the transverse plane that is close to the edges of the nuclei.

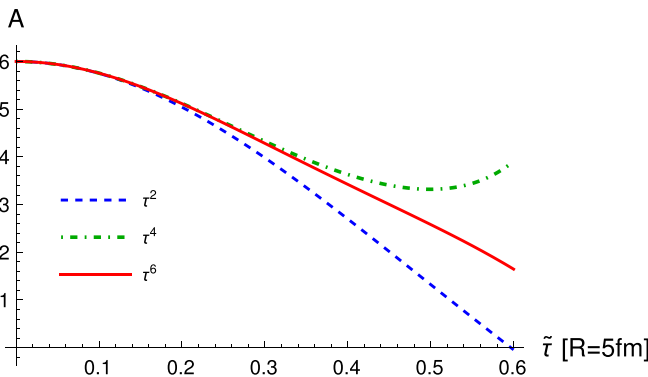


FIG. 4. The quantity A_{TL} at $R = 5$ fm and $\eta = 0$ for three different orders in the τ expansion.

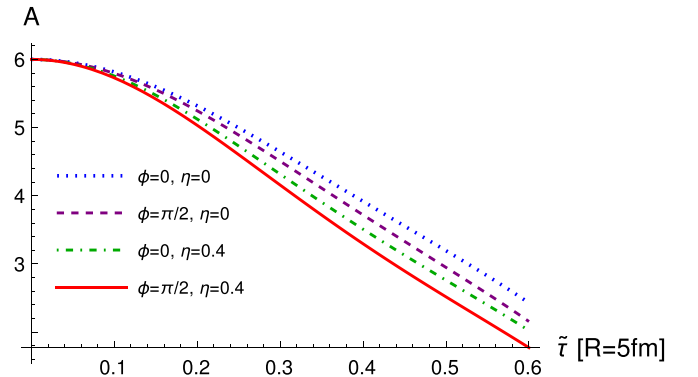


FIG. 5. The quantity A_{TL} defined in Eq. (31) at $R = 5$ fm and $b = 6$ fm.

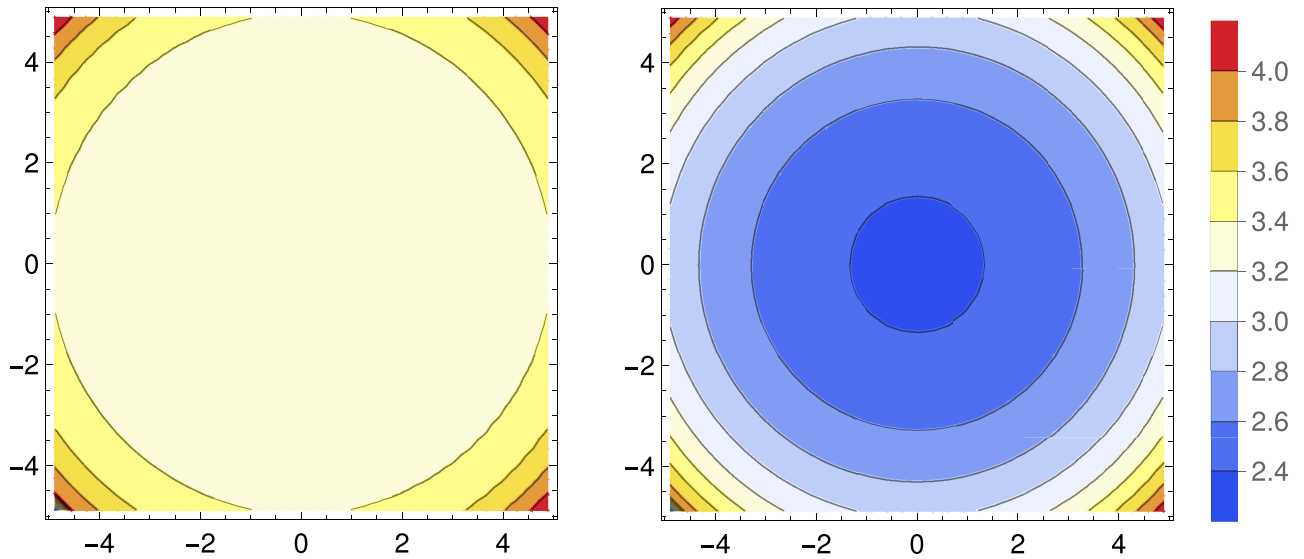


FIG. 6. The quantity A_{TL} in Eq. (31) with $b = 0$ and $\eta = 0$ at $\tau = 0.045$ fm at order τ^4 (left panel) and τ^6 (right panel). The axes show R_x and R_y in fm.

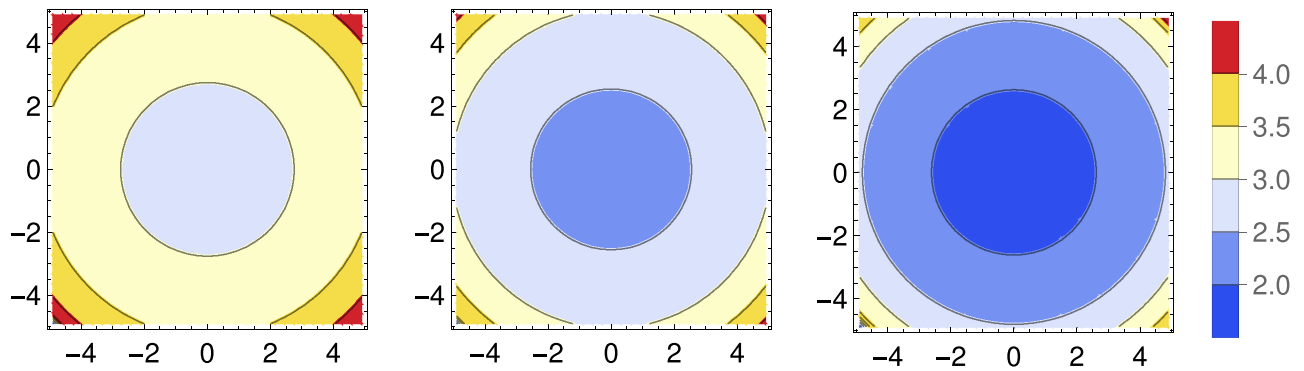


FIG. 7. The quantity A_{TL} in Eq. (31) with $b = 0$ and $\eta = 0$ at order τ^6 for $\tau = 0.04$ fm (left panel), $\tau = 0.045$ fm (center panel), and $\tau = 0.05$ fm (right panel). The axes show R_x and R_y in fm.

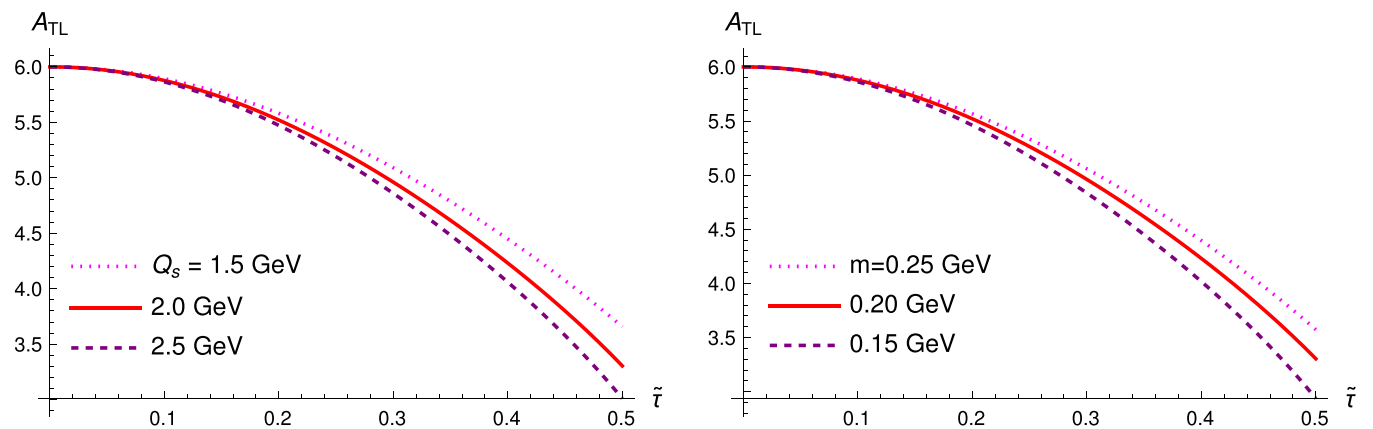


FIG. 8. The quantity A_{TL} with $R = 5$ fm, $b = 0$, and $\eta = 0$ at order τ^6 for three different values of the saturation scale (left panel) and mass parameter (right panel).

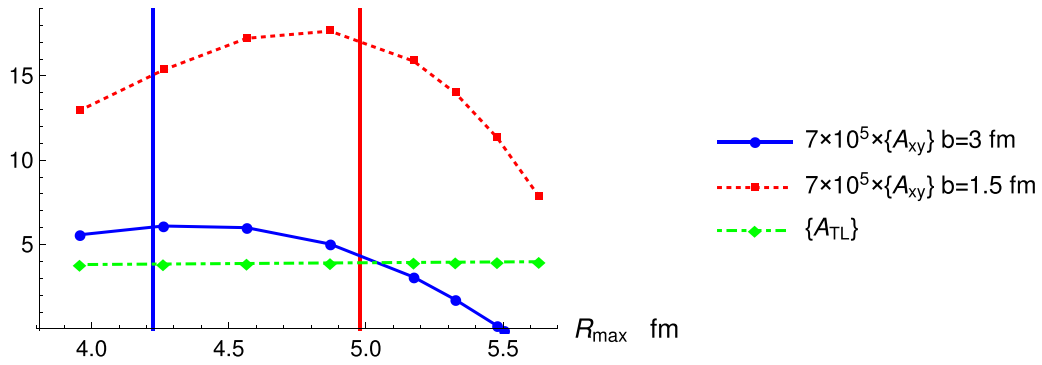


FIG. 9. The quantities $\{A_{\tau L}\}$ and $7 \times 10^5 \times \{A_{xy}\}$ at $\tau = 0.04$ fm and $\eta = 0$ as functions of R_{max} .

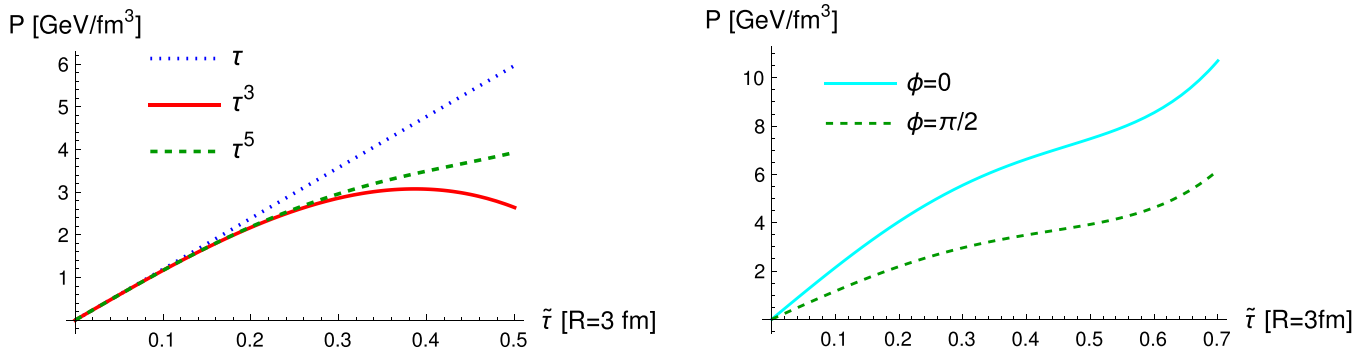


FIG. 10. The radial flow at $\eta = 0$, $b = 6$ fm, and $R = 3$ fm. The left panel shows different orders in the proper time expansion at $\phi = \pi/2$, and the right panel shows two different values of the azimuthal angle at order τ^5 .

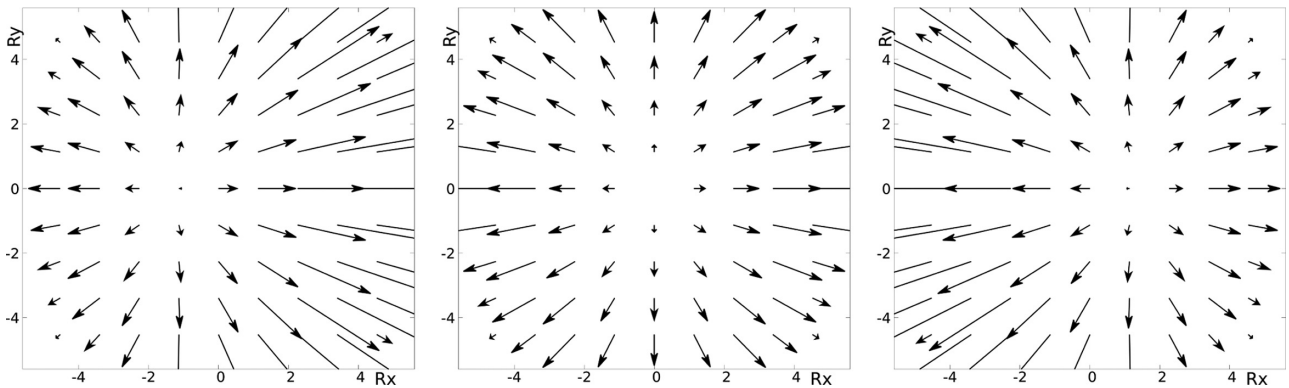


FIG. 11. The Poynting vector in the transverse plane with $b = 6$ fm and $\tau = 0.05$ fm for $\eta = -1.0$ (left), $\eta = 0$ (center), and $\eta = 1.0$ (right).

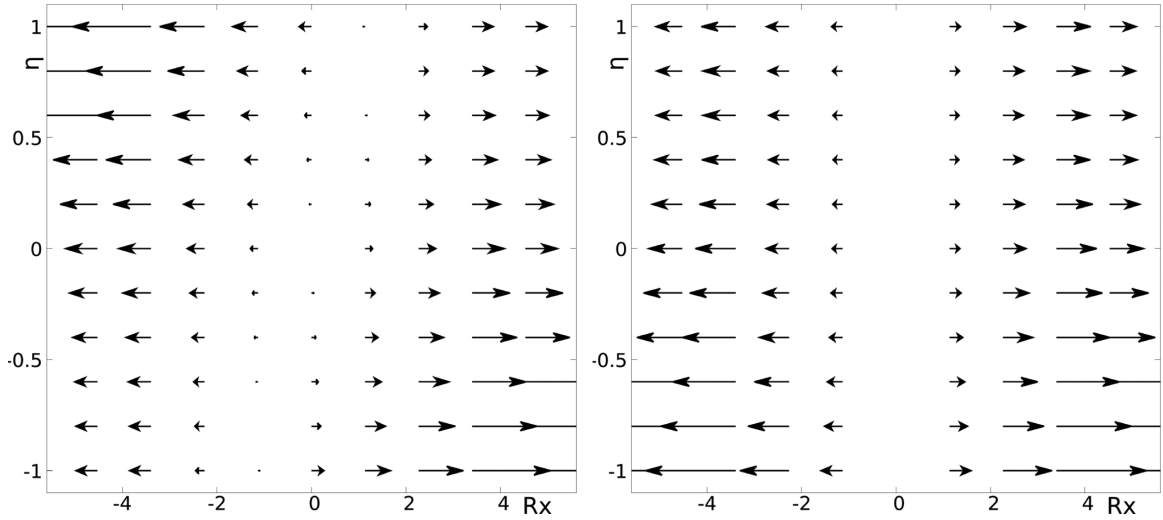


FIG. 12. The components of the Poynting vector at $\tau = 0.05$ fm with $R_y = 0$ and $A_1 = 207$ for $b = 6$ fm and $A_2 = 207$ (left panel) and for $b = 0$ and $A_2 = 40$ (right panel). The axes show R_x in fm and η .

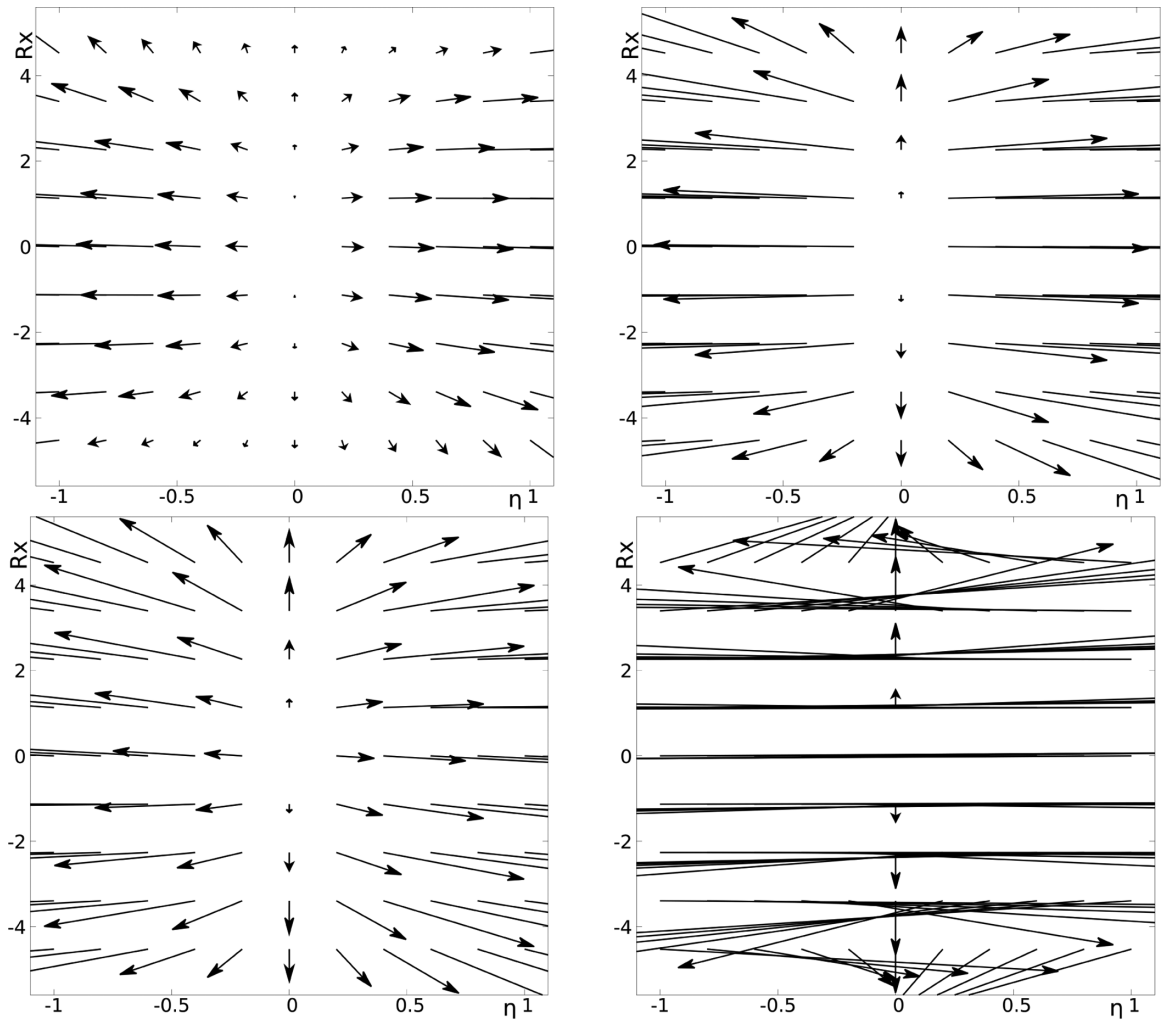


FIG. 13. The vector field $(T^{z0}, 10 T^{x0})$ with $b = 6$ fm and $R_y = 0$. The times are $\tilde{\tau} = 0.1$ (top left), $\tilde{\tau} = 0.4$ (top right), $\tilde{\tau} = 0.6$ (bottom left), and $\tilde{\tau} = 0.8$ (bottom right). At early times the motion is predominantly longitudinal, and transverse velocity components develop at later times. The last figure is beyond the time at which we trust the near field expansion.

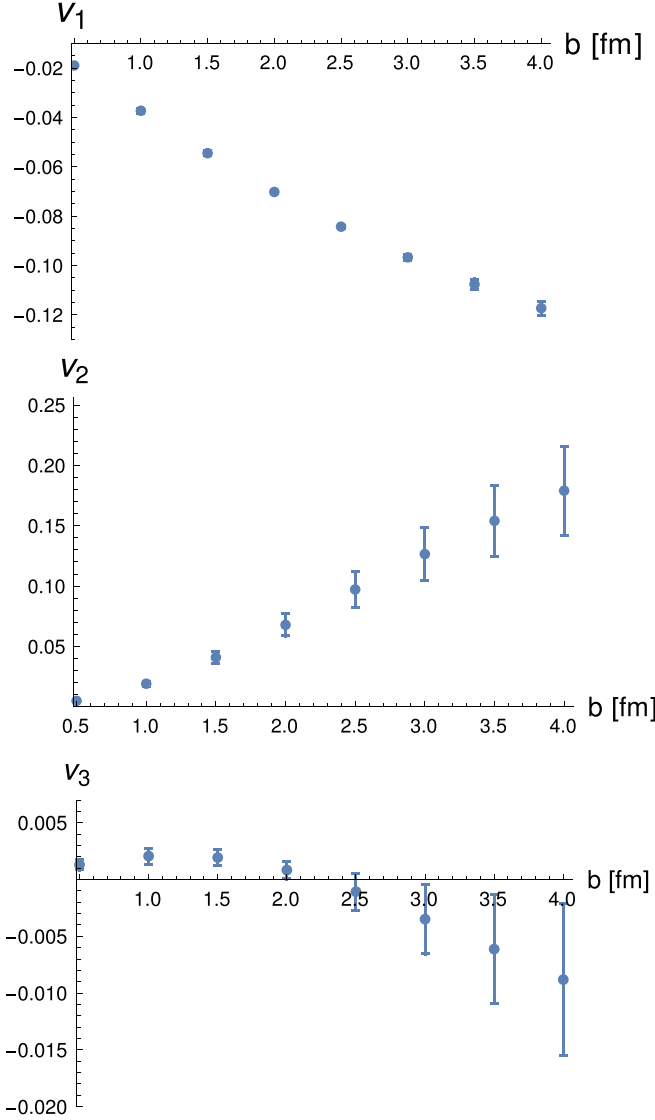


FIG. 14. The Fourier coefficients v_1 , v_2 , and v_3 with $\eta = 0.5$ and $\tau = 0.04$ fm as functions of impact parameter. The procedure for calculating the error bars is explained in the text.

We must verify that the integral is largely independent of the upper limit that is used to perform the two-dimensional integration over the transverse plane, which we call R_{\max} . In Fig. 9 we show $\{A_{xy}\}$ at $\tau = 0.04$ fm for two different values of impact parameter, as a function of R_{\max} . The two vertical lines in the figure represent the values of R_{\max} , for each value of b , for which the parameter δ in Eq. (9) is less than 0.6 for both nuclei. One sees that the result for $\{A_{xy}\}$ grows as R_{\max} increases, up to approximately the value of R_{\max} at which the gradient expansion breaks down. Smaller impact parameters give results that can be trusted up to larger values of R_{\max} , as explained in Sec. IV B. On the same graph we show the result for $\{A_{TL}\}$ at $\tau = 0.04$ fm and $\eta = 0$. The change with impact parameter is too small to be seen on the graph, and the result is almost six orders of magnitude larger than $\{A_{xy}\}$ and nearly completely independent of R_{\max} . Figure 9 clearly illustrates the problem discussed in Sec. IV B. The nature of the gradient

expansion makes it difficult to calculate any quantity that gets important contributions from the region of the transverse plane that corresponds to the edges of the nuclei. We will return to this point in Secs. IV F–IV H.

E. Radial flow

To describe the radial flow of the expanding glasma in the transverse plane, we look at the radial projection of the transverse Poynting vector $P \equiv \hat{R}^i T^{i0}$. In the left panel of Fig. 10 we show this quantity at $\eta = 0$, $b = 6$ fm, $R = 5$ fm, and $\phi = \pi/2$ at different orders in the τ expansion. At lowest order P increases linearly with time. Including higher order contributions we see that P increases more slowly with time as the system expands. If we keep only terms at order τ^3 , it appears that P actually starts to decrease when $\tilde{\tau} \gtrsim 0.4$; however, the near field expansion is not valid for these times when only terms up to cubic order are included. The result at order τ^5 shows a less pronounced flattening up to about $\tilde{\tau} = 0.5$, which again indicates the limit of validity of the near field expansion. In the right panel of Fig. 10 we show P at $\eta = 0$, $b = 6$ fm, and $R = 5$ fm for $\phi = 0$, which corresponds to \vec{R} in the reaction plane, and $\phi = \pi/2$, where \vec{R} is perpendicular to the reaction plane. One sees that the flattening is more pronounced when the azimuthal angle is smaller.

Figures 11–13 show the Poynting vector in arbitrary units in the transverse plane for $b = 6$ fm and $\tau = 0.05$ fm. The three panels in Fig. 11 correspond to three different values of fixed rapidity. One sees that for positive (negative) values of rapidity, the center of the collision moves towards the ion moving in the positive (negative) z direction which has been displaced in the positive (negative) x -direction. The positions where the magnitude of the Poynting vector is zero for the three cases shown are $(R_x, R_y) = (0, -0.91)$ fm for $\eta = -1.0$, $(0, 0)$ for $\eta = 0$, and $(0, 0.91)$ fm for $\eta = 1.0$.

In Fig. 12 we show the Poynting vector at $R_y = 0$ in the (η, R_x) plane, in arbitrary units. In the first panel we see that when η is positive, which corresponds to a position closer to the right moving ion that has been displaced in the positive x direction, the sign of the Poynting vector is predominantly negative. This corresponds to the negative value of the directed flow coefficient discussed in Sec. IV F. The second panel shows that the system expands more strongly in the wake of the larger nucleus.

In Fig. 13 we show the vector field $(T^{z0}, 10 T^{x0})$ with $b = 6$ fm and $R_y = 0$, in arbitrary units. One sees the transverse velocity components develop up until the time at which the τ expansion breaks down.

F. Fourier coefficients of the azimuthal distribution

In this section we calculate Fourier coefficients of the azimuthal distribution of the flow vector $T^{i0}(\vec{x}_\perp)$. The flow vectors are used as input in hydrodynamic codes, and the Fourier coefficients are related to experimental observables. In Appendix C we define the form of the azimuthal distribution

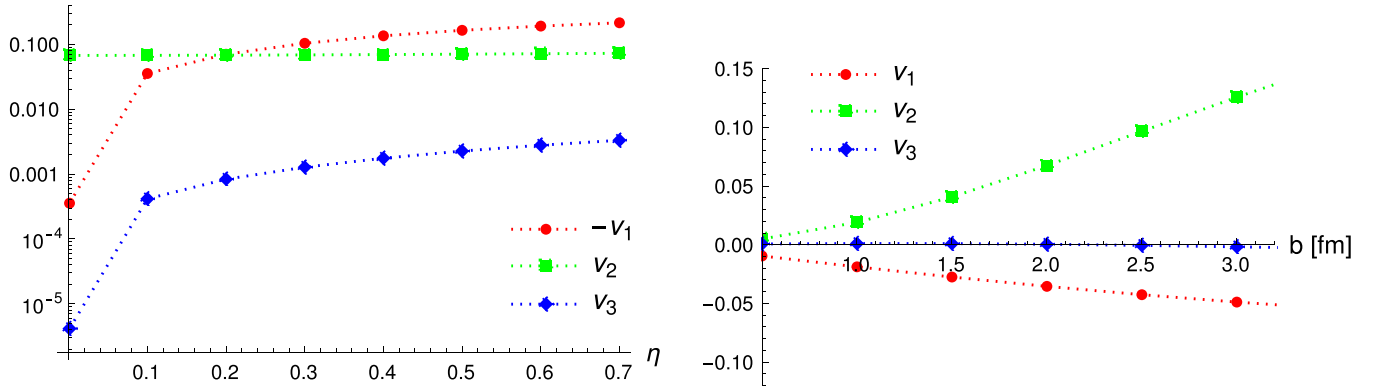


FIG. 15. The Fourier coefficients v_1 , v_2 , and v_3 at $\tau = 0.04$ fm. The left panel is for fixed $b = 2$ fm and the right panel is fixed $\eta = 0.1$.

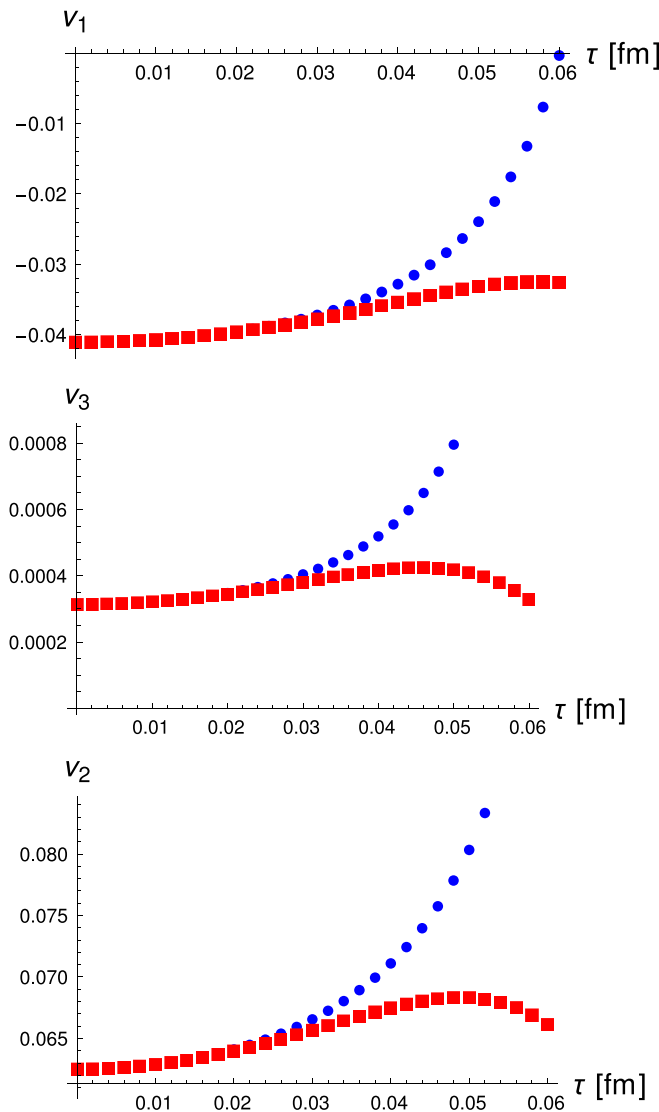


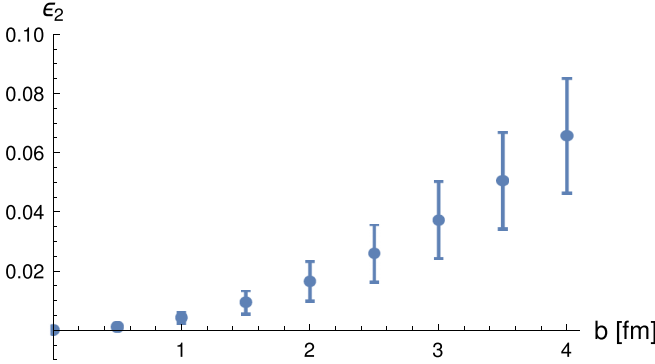
FIG. 16. The Fourier coefficients v_1 , v_2 , and v_3 at $\eta = 0.1$ and $b = 2$ fm as functions of time. The blue dots show the result at order τ^3 and the red squares represent the order τ^5 results.

that we use and explain how the Fourier coefficients v_n are calculated.

We note that among the important sources of uncertainty in experimentally determined values of Fourier coefficients are fluctuations in the positions of the nucleons that directly participate in the primary interaction, which produce deviations between the orientation of the event plane, determined by the principal axes of the participants, and the reaction plane. In our calculation the reaction plane is known, and fluctuations are not included. One consequence is that the Fourier coefficients in our calculation exhibit specific symmetries: the coefficients v_n with n odd are rapidity odd, and those with n even are rapidity even.

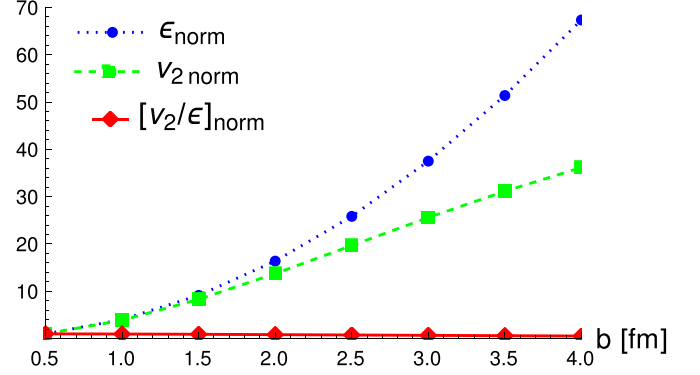
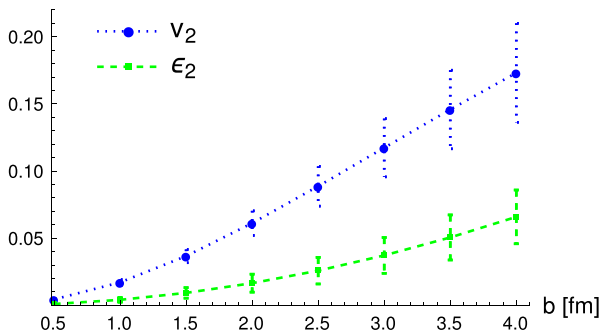
To estimate the error in the Fourier coefficients, we perform the integrals using, for each value of b , a set of 15 evenly spaced values of R_{\max} between 4.5 and 7.0 fm. We average the results and calculate the error bar from the standard deviation. In Fig. 14 we show the first three Fourier coefficients at $\eta = 0.5$ and $\tau = 0.04$ fm. As in Sec. IVD 2, we find that the calculation is reasonably insensitive to the upper limit of the integration for impact parameters $b \lesssim 2.5$ fm.

In Fig. 15 we look at the first three Fourier coefficients as functions of rapidity and impact parameter, at $\tau = 0.04$ fm. We use $R_{\max} = 5.9$ fm in all calculations. In the left panel of figure 15 we show v_1 , v_2 , and v_3 at $\tau = 0.04$ fm with $b = 2$ fm as a function of rapidity. In the right panel we show the same three Fourier coefficients at $\tau = 0.04$ fm and $\eta = 0.1$ as functions of impact parameter. The directed flow coefficient, v_1 , is negative (for $\eta > 0$), and the elliptic flow coefficient, v_2 , is positive. The triangle coefficient v_3 is small and positive (for $\eta > 0$) when $b \lesssim 2$ fm. In Fig. 16 we show v_1 , v_2 , and v_3 as functions of time with $\eta = 0.1$ and $b = 2$ fm, at order τ^3 and order τ^5 . In all cases the curves agree well at small times. The order τ^3 curves bend sharply upward at $\tau \approx 0.03$ fm, which shows the breakdown of the τ expansion at third order. At larger values of τ , the order τ^5 results show the opposite behavior, bending rapidly downward. Similar behavior is seen in Fig. 4 and is discussed in Sec. IVD 1. We determine numerically that the position of the peak for each of the three curves that show order τ^5 results is $\tau \approx 0.05$ fm, which is


 FIG. 17. The eccentricity ε_2 as a function of impact parameter.

approximately the time at which the expansion breaks down. The time for which the second derivative is zero, which corresponds to the point where the curves start to flatten, is approximately $\tau \approx 0.03$ fm for all three curves. This flattening of all three curves inside the region where the τ expansion converges provides some evidence that the Fourier coefficients will not change rapidly immediately outside the region of validity of the near field expansion. We also comment that the radial flow shows similar behavior (see Fig. 10).

Our results for the second and third Fourier coefficients are of the same order as experimental values [26,27], although our result for $|v_1|$ is much bigger than expected [28]. However, it is usually assumed that anisotropy develops mostly during the hydrodynamic evolution that follows the glasma phase, and in this context our results are surprisingly large for all three Fourier coefficients. Azimuthal correlations in glasma have been investigated by several other groups, using different approaches and looking at different regimes, which makes comparison difficult. In Ref. [25] the authors use a different method and consider impact parameters that are larger than the maximum value for which the gradient expansion can be trusted, and times that are beyond the validity of the near field expansion, but still obtain smaller values of v_2 . In Refs. [29,30] the origins of azimuthal correlations in the CGC approach are studied, but quantitative results for a glasma system are not obtained.


 FIG. 19. The eccentricity ε_2 , the elliptic flow coefficient v_2 , and their ratio at $\tau = 0.04$ fm and $\eta = 0$ with all curves normalized so that the value at $b = 0.5$ fm is set to 1.

G. Eccentricity

Spatial deviations from azimuthal symmetry can be characterized with the quantity [31,32]

$$\varepsilon_n = -\frac{\int d^2\vec{R}|\vec{R}|\cos(n\phi)\mathcal{E}(\vec{R})}{\int d^2\vec{R}|\vec{R}|\mathcal{E}(\vec{R})} \quad \text{with } \phi = \tan^{-1}(R_y/R_x), \quad (34)$$

where $\mathcal{E}(\vec{R})$ denotes the energy density.² In Fig. 17 we show the eccentricity, ε_2 , as a function of impact parameter at $\tau = 0.04$ fm and $\eta = 0$. The error bars are calculated from the standard deviation of the results obtained using 15 values of R_{\max} that are evenly spaced between 4.5 and 7.0 fm. The results show that ε_2 is largely insensitive to R_{\max} for impact parameters $b \lesssim 2.5$ fm. In Fig. 18 we show v_2 , ε_2 , and v_2/ε_2 at $\tau = 0.04$ fm and $\eta = 0$ using $R_{\max} = 5.9$ fm. In Fig. 19 we show the same curves normalized so that the value at $b = 0.5$ fm is set to 1. The results show a clear correlation between the spatial asymmetry introduced by the initial geometry, and the anisotropy of the azimuthal distribution of the gluon momentum. Correlations of this kind are considered characteristic of the onset of hydrodynamic behavior.

²The sign in Eq. (34) is chosen to agree with Eq. (44) of Ref. [33].

 FIG. 18. The left panel shows the elliptic flow coefficient v_2 and the eccentricity ε_2 , and the right panel shows their ratio. All results are at $\tau = 0.04$ fm and $\eta = 0$.

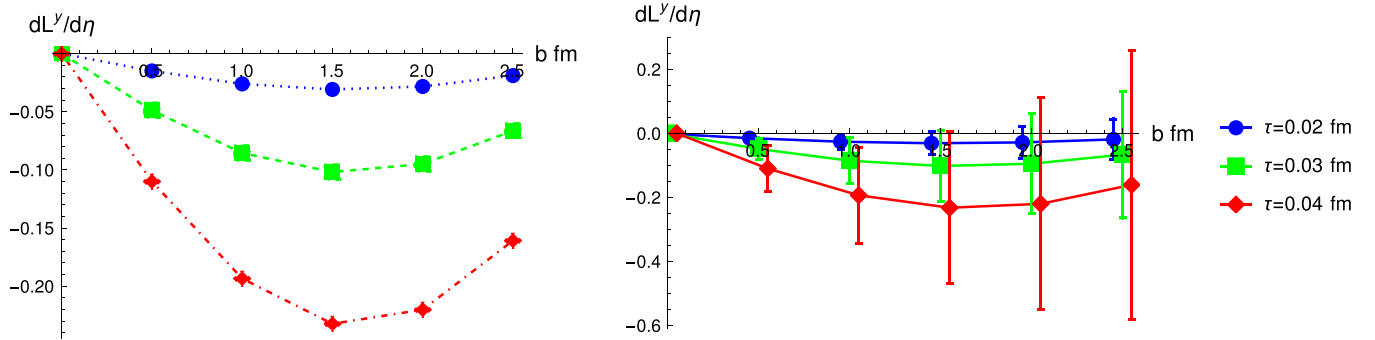


FIG. 20. The angular momentum per unit rapidity as a function of impact parameter. The right panel shows the same three curves as in the left panel but with error bars included, and the values of impact parameter are shifted 0.05 fm left for the $\tau = 0.02$ fm curve, and 0.05 fm right for the $\tau = 0.04$ fm curve, so that the error bars are separated enough to be seen individually.

H. Angular momentum

The angular momentum of the glasma can be calculated from Eq. (28). In the left panel of Fig. 20 we show our results at three different times, using $R_{\max} = 5.9$ fm. The error bars in the right panel are obtained by calculating the standard deviation of the results using a set of evenly spaced values for R_{\max} between 4.5 and 7.0 fm. The error bars that are produced by this procedure are large, even for small impact parameters (for comparison see Figs. 14 and 17). This happens because the problem discussed in Sec. IV B is much more serious in the calculation of angular momentum than it was in Secs. IV F and IV G. The dominant contribution to the angular momentum comes from the parts of the nuclei that are farthest from the collision center, with respect to which angular momentum is calculated, but these are the regions where the gradient expansion is least to be trusted. The angular momentum is negative, which is expected when the ions moving in the positive (negative) z directions are displaced in the positive (negative) x directions. We note that in spite of the size of the error bars in Fig. 20, the general shape of the curves is consistently reproduced when the value of R_{\max} is changed. Furthermore, this shape matches the basic form of the results in Refs. [21,22]. It is especially interesting that in all three calculations, the peak occurs at ≈ 2.0 – 2.5 fm, which is within the range of impact parameters where the gradient expansion

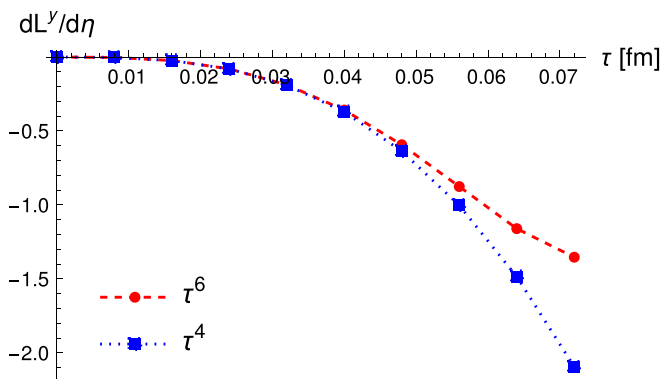


FIG. 21. The angular momentum per unit rapidity as a function of proper time with $b = 2$ fm using $R_{\max} = 5.9$ fm.

that we use can be trusted. However, it is important to note that the values for angular momentum obtained in [21,22] are $\approx 10^5$ at RHIC energies, and even larger at LHC energies, and are thus five to six orders of magnitude larger than our results.

In Fig. 21 we show the angular momentum as a function of proper time, at fixed impact parameter $b = 2$ fm at different orders in the τ expansion. We have used the value $R_{\max} = 5.9$ fm in all cases. The figure shows that the τ expansion appears to converge for much larger times than the other quantities we have calculated. The authors of Ref. [8] observed that the near field expansion method can produce very large values of angular momentum, if one considers large enough times. We have verified that our calculation reproduces this behavior, but the sign of the angular momentum changes, and the numerical value of the result depends strongly on the order of the τ expansion. Both of these properties indicate that there is no reason to believe the result is physical.

Our results indicate that the glasma carries only a very small imprint of the primordial angular momentum, which means that the majority of the angular momentum is carried by valence quarks, for times at which the calculation is valid. This result casts doubt on the idea of a rapidly rotating initial glasma state that could be observed via polarization of final state hadrons.

V. CONCLUSIONS

We have used a CGC approach and an expansion in proper time to derive an analytic result for the glasma energy-momentum tensor to sixth order in the proper time. We have taken into account some aspects of nuclear structure using spatially dependent nuclear density functions. In our previous paper [3] we gave a detailed description of the steps involved in our calculation. In this paper, we have concentrated on the physical results that can be obtained from our final expression for the energy-momentum tensor.

For most of the quantities that we calculated, the proper time expansion can be trusted to about $\tau = 0.05$ fm, and we have shown that the glasma moves towards equilibrium until the time at which the near field expansion breaks down. Using simple arguments based on the uncertainty principle [3], one can argue that this upper bound of the region where the near field expansion converges reaches far beyond the lower

bound at which we no longer trust the classical description that is inherent in our method. Our calculation also requires an expansion in gradients of the nuclear density function. Some of the quantities we have calculated are almost entirely insensitive to this expansion, and in other cases the gradient expansion restricts us to the consideration of small impact parameters.

We have calculated the first three Fourier coefficients of the azimuthal distribution of the momentum field of the glasma. Our results are larger than is generally expected, which is interesting because it contradicts the usual assumption that azimuthal anisotropy is mostly generated during the hydrodynamic evolution of the plasma. We have also calculated the eccentricity of the glasma, which describes the spatial azimuthal asymmetry of the system. We have found a sizable correlation between the elliptic flow coefficient and the eccentricity, which indicates that the spatial asymmetry introduced by the initial geometry is effectively transmitted to the azimuthal distribution of the gluon momentum field. This result is interesting because a correlation of this kind is an indication of the onset of hydrodynamics. We have formulated a calculation of the angular momentum per unit rapidity, on a hypersurface of constant proper time. Our results are much smaller than the total angular momentum of the participating nucleons [21,22,28], which shows that most of the angular momentum carried by valence quarks is not transmitted to the glasma. These results are significant because they contradict the picture of a rapidly rotating initial glasma state that has been proposed by several authors [9,10] and led to experimental searches for a polarization effect in the hyperons and vector mesons produced in heavy ion collisions, which have been, so far, largely unsuccessful [11,12].

Finally, we comment that all of the calculation done in this paper make use of analytic solutions of the near field expanded YM equation which we have obtained to order τ^6 , and these results are also useful in other contexts. We are currently

using these solutions to perform a calculation of the transport properties of heavy quarks in glasma.

ACKNOWLEDGMENTS

This work was partially supported by the Natural Sciences and Engineering Research Council of Canada from Grant No. 2017-00028 and National Science Centre, Poland under Grant No. 2018/29/B/ST2/00646.

APPENDIX A: NOTATION

The collision axis is defined to be the z axis and the two transverse coordinates are denoted \vec{x}_\perp . We use Minkowski, light-cone, and Milne coordinates in different parts of the calculation, and these coordinates are written (t, z, \vec{x}_\perp) , $(x^+, x^-, \vec{x}_\perp)$, and $(\tau, \eta, \vec{x}_\perp)$. We use the conventional definitions

$$x^+ = \frac{t+z}{\sqrt{2}} \quad \text{and} \quad x^- = \frac{t-z}{\sqrt{2}}, \quad (\text{A1})$$

$$\tau = \sqrt{t^2 - z^2} = \sqrt{2x^+x^-} \quad \text{and} \quad \eta = \frac{1}{2} \ln \left(\frac{x^+}{x^-} \right). \quad (\text{A2})$$

We define the relative and average transverse coordinates

$$\vec{r} = \vec{x}_\perp - \vec{y}_\perp \quad \text{and} \quad \vec{R} = \frac{1}{2}(\vec{y}_\perp + \vec{x}_\perp). \quad (\text{A3})$$

We will write unit vectors as $\hat{r} = \vec{r}/|\vec{r}| = \vec{r}/r$ and $\hat{R} = \vec{R}/|\vec{R}| = \vec{R}/R$ and use standard notation for derivatives, for example

$$\partial_x^i = -\nabla_x^i = -\frac{\partial}{\partial x_\perp^i}, \quad (\text{A4})$$

and similarly for y_\perp , \vec{r} , and \vec{R} .

The metric tensors in these three coordinate systems are $g^{\text{mink}} = (1, -1, -1, -1)_{\text{diag}}$ and

$$g_{\mu\nu}^{\text{lc}} = \begin{pmatrix} 0 & 1 & 0 & 0 \\ 1 & 0 & 0 & 0 \\ 0 & 0 & -1 & 0 \\ 0 & 0 & 0 & -1 \end{pmatrix}, \quad g_{\mu\nu}^{\text{milne}} = \begin{pmatrix} 1 & 0 & 0 & 0 \\ 0 & -\tau^2 & 0 & 0 \\ 0 & 0 & -1 & 0 \\ 0 & 0 & 0 & -1 \end{pmatrix}. \quad (\text{A5})$$

The coordinate transformations are

$$x_{\text{mink}}^\mu = M_\nu^\mu x_{\text{lc}}^\nu, \quad M_\nu^\mu = \frac{dx_{\text{mink}}^\mu}{dx_{\text{lc}}^\nu} = \begin{pmatrix} \frac{1}{\sqrt{2}} & \frac{1}{\sqrt{2}} & 0 & 0 \\ \frac{1}{\sqrt{2}} & -\frac{1}{\sqrt{2}} & 0 & 0 \\ 0 & 0 & 1 & 0 \\ 0 & 0 & 0 & 1 \end{pmatrix},$$

$$x_{\text{mink}}^\mu = M_\nu^\mu x_{\text{milne}}^\nu, \quad M_\nu^\mu = \frac{dx_{\text{mink}}^\mu}{dx_{\text{milne}}^\nu} = \begin{pmatrix} \cosh(\eta) & \tau \sinh(\eta) & 0 & 0 \\ \sinh(\eta) & \tau \cosh(\eta) & 0 & 0 \\ 0 & 0 & 1 & 0 \\ 0 & 0 & 0 & 1 \end{pmatrix}. \quad (\text{A6})$$

The generators t_a of $SU(N_c)$ satisfy

$$\begin{aligned} [t_a, t_b] &= if_{abc}t_c, \\ \text{Tr}(t_a t_b) &= \frac{1}{2}\delta_{ab}, \\ f_{abc} &= -2i\text{Tr}(t_a[t_b, t_c]). \end{aligned} \quad (\text{A7})$$

Functions like A_μ , J_μ , ρ , and Λ are $SU(N_c)$ valued functions and can be written as linear combinations of the $SU(N_c)$ generators. In the adjoint representation we write the generators with a tilde as $(\tilde{t}_a)_{bc} = -if_{abc}$.

APPENDIX B: COEFFICIENTS OF THE ENERGY-MOMENTUM TENSOR AT ORDER τ^4

In this Appendix we give the coefficients \mathcal{X}_n^{lm} of Eq. (18) with $n = 4$. We remind the reader of the notation we are using. We have defined $L \equiv \ln(Q_s/m)$, $\hat{\mu}_1(\vec{R}) \equiv \mu_1(\vec{R})/\bar{\mu}$, $\hat{\mu}_2(\vec{R}) \equiv \mu_2(\vec{R})/\bar{\mu}$, $\bar{\mu} \equiv Q_s^2/g^4$, and we use the shorthand notation $\hat{\mu}_1^{10} \equiv \nabla_x \hat{\mu}_1(\vec{R})$, $\hat{\mu}_1^{11} \equiv \nabla_x \nabla_y \hat{\mu}_1(\vec{R})$, etc. Our fourth-order results are

$$\begin{aligned} \beta_4^{10} &= \frac{\hat{\mu}_1 Q_s^8}{65536\pi^4 g^2} (-9\hat{\mu}_2^2(1-2L)^4(5828\hat{\mu}_1^{10} - 3449\hat{\mu}_2^{10}) - 46800\pi\hat{\mu}_2(1-2L)^2\hat{\mu}_1^{10} \\ &\quad + [-31041\hat{\mu}_1^2(1-2L)^4 - 48240\pi\hat{\mu}_1(1-2L)^2 + 5120\pi^2(L+1)]\hat{\mu}_2^{10}) - (\hat{\mu}_1 \leftrightarrow \hat{\mu}_2), \\ \gamma_4^{11} &= -\frac{27\hat{\mu}_1 Q_s^8}{32768\pi^4 g^2 m^2} ((2L-1)\{\hat{\mu}_2^2(1-2L)^2(287\hat{\mu}_1^{11} + 216\hat{\mu}_2^{11}) \\ &\quad + \hat{\mu}_1[175\hat{\mu}_1(1-2L)^2 + 144\pi]\hat{\mu}_2^{11} + 216\pi\hat{\mu}_2\hat{\mu}_1^{11}\}) + (\hat{\mu}_1 \leftrightarrow \hat{\mu}_2), \\ \delta_4^{02} &= \frac{3\hat{\mu}_1 Q_s^8}{65536\pi^4 g^2 m^2} (9\hat{\mu}_2^2(2L-1)^3(2443\hat{\mu}_1^{02} + 2530\hat{\mu}_2^{02}) + 16080\pi\hat{\mu}_2(2L-1)\hat{\mu}_1^{02} \\ &\quad + [9951\hat{\mu}_1^2(2L-1)^3 + 8496\pi\hat{\mu}_1(2L-1) + 256\pi^2]\hat{\mu}_2^{02}) + (\hat{\mu}_1 \leftrightarrow \hat{\mu}_2), \\ \delta_4^{20} &= \frac{3\hat{\mu}_1 Q_s^8}{65536\pi^4 g^2 m^2} (9\hat{\mu}_2^2(2L-1)^3(1869\hat{\mu}_1^{20} + 2098\hat{\mu}_2^{20}) + 12192\pi\hat{\mu}_2(2L-1)\hat{\mu}_1^{20} \\ &\quad + [6801\hat{\mu}_1^2(2L-1)^3 + 5904\pi\hat{\mu}_1(2L-1) + 256\pi^2]\hat{\mu}_2^{20}) + (\hat{\mu}_1 \leftrightarrow \hat{\mu}_2), \\ \mathcal{E}_4^{00} &= \frac{3\hat{\mu}_1\hat{\mu}_2 Q_s^8}{65536\pi^4 g^2} (8376\hat{\mu}_2^2(1-2L)^4 + 3\hat{\mu}_2[1797\hat{\mu}_1(1-2L)^2 + 3904\pi](2L-1)^2 + 256\pi^2(2L+3)) + (\hat{\mu}_1 \leftrightarrow \hat{\mu}_2), \\ \mathcal{E}_4^{02} &= \frac{\hat{\mu}_1 Q_s^8}{32768\pi^4 g^2 m^2} (9\hat{\mu}_2^2(2L-1)^3(1078\hat{\mu}_1^{02} + 1157\hat{\mu}_2^{02}) + 7068\pi\hat{\mu}_2(2L-1)\hat{\mu}_1^{02} \\ &\quad + 4([1047\hat{\mu}_1^2(2L-1)^3 + 900\pi\hat{\mu}_1(2L-1) + 32\pi^2]\hat{\mu}_2^{02}) + (\hat{\mu}_1 \leftrightarrow \hat{\mu}_2). \end{aligned} \quad (\text{B1})$$

APPENDIX C: AZIMUTHAL DISTRIBUTION

In this section we define the azimuthal distribution of the flow vector $T^{i0}(\vec{x}_\perp)$. The azimuthal angle is measured with respect to the x axis and is written as

$$\varphi(\vec{x}_\perp) = \tan^{-1} \left(\frac{T^{0y}(\vec{x}_\perp)}{T^{0x}(\vec{x}_\perp)} \right) = \cos^{-1} \left(\frac{T^{0x}(\vec{x}_\perp)}{\sqrt{[T^{0x}(\vec{x}_\perp)]^2 + [T^{0y}(\vec{x}_\perp)]^2}} \right). \quad (\text{C1})$$

We define the distribution

$$P(\phi) \equiv \frac{1}{\Omega} \int d^2\vec{x}_\perp \delta(\phi - \varphi(\vec{x}_\perp)) W(\vec{x}_\perp), \quad (\text{C2})$$

where we have introduced the weighting function

$$W(\vec{x}_\perp) \equiv \sqrt{[T^{0x}(\vec{x}_\perp)]^2 + [T^{0y}(\vec{x}_\perp)]^2} \quad (\text{C3})$$

and the normalization factor

$$\Omega \equiv \int d^2\vec{x}_\perp W(\vec{x}_\perp). \quad (\text{C4})$$

The distribution $P(\phi)$ can be decomposed into Fourier harmonics as

$$P(\phi) = \frac{1}{2\pi} \left(1 + 2 \sum_{n=1}^{\infty} v_n \cos(n\phi) \right), \quad (C5)$$

where coefficients v_n are given by the relation

$$v_n = \int_0^{2\pi} d\phi \cos(n\phi) P(\phi). \quad (C6)$$

-
- [1] F. Gelis, E. Iancu, J. Jalilian-Marian, and R. Venugopalan, *Annu. Rev. Nucl. Part. Sci.* **60**, 463 (2010).
- [2] T. Lappi, *Int. J. Mod. Phys. E* **20**, 1 (2011).
- [3] M. E. Carrington, A. Czajka, and St. Mrówczyński, *Eur. Phys. J. A* **58**, 5 (2022).
- [4] R. J. Fries, J. I. Kapusta, and Y. Li, *Nucl. Phys. A* **774**, 861 (2006).
- [5] K. Fukushima, *Phys. Rev. C* **76**, 021902(R) (2007).
- [6] H. Fujii, K. Fukushima, and Y. Hidaka, *Phys. Rev. C* **79**, 024909 (2009).
- [7] G. Chen, R. J. Fries, J. I. Kapusta, and Y. Li, *Phys. Rev. C* **92**, 064912 (2015).
- [8] R. J. Fries, G. Chen, and S. Somanathan, *Phys. Rev. C* **97**, 034903 (2018).
- [9] Z. T. Liang and X. N. Wang, *Phys. Lett. B* **629**, 20 (2005).
- [10] Z. T. Liang, M. A. Lisa, and X. N. Wang, *Nucl. Phys. News* **30**, 10 (2020).
- [11] J. Adam *et al.* (STAR Collaboration), *Phys. Rev. C* **98**, 014910 (2018).
- [12] S. Acharya *et al.* (ALICE Collaboration), *Phys. Rev. C* **101**, 044611 (2020).
- [13] A. Kovner, L. D. McLerran, and H. Weigert, *Phys. Rev. D* **52**, 3809 (1995).
- [14] J. P. Blaizot, F. Gelis, and R. Venugopalan, *Nucl. Phys. A* **743**, 57 (2004).
- [15] K. Fukushima and Y. Hidaka, *J. High Energy Phys.* **06** (2007) 040.
- [16] J. L. Albacete, P. Guerrero-Rodríguez, and C. Marquet, *J. High Energy Phys.* **01** (2019) 073.
- [17] F. Fillion-Gourdeau and S. Jeon, *Phys. Rev. C* **79**, 025204 (2009).
- [18] T. Lappi and S. Schlichting, *Phys. Rev. D* **97**, 034034 (2018).
- [19] J. Jalilian-Marian, A. Kovner, L. D. McLerran, and H. Weigert, *Phys. Rev. D* **55**, 5414 (1997).
- [20] E. Iancu and R. Venugopalan, in *Quark-Gluon Plasma 3*, edited by R. C. Hwa and X.-N. Wang (World Scientific, Singapore, 2004).
- [21] J. H. Gao, S. W. Chen, W. T. Deng, Z. T. Liang, Q. Wang, and X. N. Wang, *Phys. Rev. C* **77**, 044902 (2008).
- [22] F. Becattini, F. Piccinini, and J. Rizzo, *Phys. Rev. C* **77**, 024906 (2008).
- [23] J. Jankowski, S. Kamata, M. Martinez, and M. Spaliński, *Phys. Rev. D* **104**, 074012 (2021).
- [24] M. Li and J. I. Kapusta, *Phys. Rev. C* **94**, 024908 (2016).
- [25] A. Krasnitz, Y. Nara, and R. Venugopalan, *Phys. Lett. B* **554**, 21 (2003).
- [26] G. Aad *et al.* (ATLAS Collaboration), *Phys. Rev. C* **86**, 014907 (2012).
- [27] U. Heinz and R. Snellings, *Annu. Rev. Nucl. Part. Sci.* **63**, 123 (2013).
- [28] I. Selyuzhenkov, *J. Phys. G: Nucl. Part. Phys.* **38**, 124167 (2011).
- [29] B. Schenke, S. Schlichting, and R. Venugopalan, *Phys. Lett. B* **747**, 76 (2015).
- [30] T. Lappi, B. Schenke, S. Schlichting, and R. Venugopalan, *J. High Energy Phys.* **01** (2016) 061.
- [31] J. P. Blaizot, W. Broniowski, and J. Y. Ollitrault, *Phys. Lett. B* **738**, 166 (2014).
- [32] S. Demirci, T. Lappi, and S. Schlichting, *Phys. Rev. D* **103**, 094025 (2021).
- [33] S. A. Voloshin, A. M. Poskanzer, and R. Snellings, in *Relativistic Heavy Ion Physics*, edited by R. Stock, Landolt-Börnstein, New Series (Springer, Berlin, 2010), Vol. 23, p. 293.